Nano-Structures & Nano-Objects 45 (2026) 101597

Contents lists available at ScienceDirect

Nano-Structures & Nano-Objects

journal homepage: www.elsevier.com/locate/nanoso

SERS sensing of the biomolecule of Palbociclib (PCB) adsorbed on Au_3 cluster: DFT, reactivity, docking and MD simulations

Jamelah S. Al-Otaibi [a], Y. Sheena Mary [b], A. Saral [c], M. Cristina Gamberini [d,*]

[a] Department of Chemistry, College of Science, Princess Nourah Bint Abdulrahman University, P.O. Box 84428, Riyadh 11671, Saudi Arabia
[b] Department of Physics, FMN College, Kollam, University of Kerala, Kerala, India
[c] Department of Chemistry, Panimalar Engineering College, Chennai, Tamil Nadu, India
[d] Department of Life Sciences, University of Modena and Reggio Emilia, via G. Campi 103, Modena 41125, Italy

ARTICLE INFO

Keywords:
SERS
Au_3 cluster
MD simulations

ABSTRACT

Understanding how anticancer drugs interact with metallic nanoclusters is essential for developing next-generation sensing and delivery platforms. In this study, we investigate the adsorption behavior, spectroscopic response, reactivity, and biological binding characteristics of Palbociclib (PCB) on a gold triatomic cluster (Au_3) using an integrated computational framework. Density functional theory (DFT) calculations reveal strong and site-selective adsorption of PCB on Au_3 accompanied by pronounced charge transfer and significant modulation of the molecule's electronic structure including reduced HOMO-LUMO gaps, enhanced polarizability, and improved nonlinear optical (NLO) characteristics. Vibrational and SERS analyses show characteristic red shifts and intensity enhancements, confirming stable coordination through key nitrogen and oxygen bearing functional groups. Solvent-phase calculations further demonstrate that PCB-Au_3 complexes gain substantial stabilization in aqueous media, reinforcing their potential in biological environments. Molecular docking and 100 ns molecular dynamics simulations with the 5GS4 protein indicate that both free PCB and PCB-Au_3 form thermodynamically favorable and dynamically stable complexes, with PCB-Au_3 exhibiting enhanced interaction diversity through hydrophobic, hydrogen-bonding, and Au-induced electronic effects. MM-GBSA analysis supports these findings, revealing competitive binding energies for both ligands. Collectively, these results highlight Au_3 nanoclusters as promising nanoscale scaffolds for SERS-based detection and controlled delivery of PCB, providing valuable insights for cancer diagnostic and theranostic applications.

1. Introduction

Because of their NLO characteristics, organometallic compounds have attracted a lot of interest and can be used in a variety of sectors, including medicine and photonics devices [1]. Due to their lower cost and simpler chemical transformation, these materials could be used as a substitute for typical inorganic NLO compounds [2]. The manufacture of metal nanoparticles with the aim of improving their surface-to-volume ratio is becoming more and more popular these days. Thus, their applications are important as analytical instruments [3,4]. For biochemical, pharmaceutical, environmental, and dietary analyses, SERS spectroscopy is a very promising alternative to traditional analytical methods. Coinage nanoparticle-based SERS has been found to be a successful technique for detecting contaminants [5]. The interactions between drugs and gold and silver, have been the subject of several investigations [6]. In the medical field, silver nanoparticles have long been used for antimicrobials, cosmetics, food preservation, textile coatings, and a few environmental uses [7–16]. Wen et al., investigated SERS analysis of carboxylic acids using SERS [17,18].

Coinage metals have unique characteristics that make them highly desirable for a range of uses [19–24]. These materials' unusual electrical topologies make them particularly intriguing in its technological importance [25–27]. Dihydropyrimidine drugs have studied for their therapeutic potential [28,29]. The oral route of pharmaceutical distribution is considered the greatest alternative available due to its affordability, safely, and patient compliance. The solubility of an active ingredient is the most important factor affecting its oral bioavailability [30]. Using drug inclusion complexes with suitable hosts is a practical strategy for improving the solubility of pharmaceuticals [31]. A cyclin-dependent kinase inhibitor called palbociclib has been authorized

* Corresponding author.
E-mail address: mariacristina.gamberini@unimore.it (M.C. Gamberini).

https://doi.org/10.1016/j.nanoso.2025.101597
Received 31 October 2025; Received in revised form 25 November 2025; Accepted 4 December 2025
Available online 10 December 2025

by the US FDA to treat breast cancer [32]. By preventing the abnormal protein that tells cancer cells to multiply from doing so, PCB helps prevent or slow the spread of cancer cells [33]. Given that breast cancer is usually the most common cancer in women and the second most common disease overall, research into PCB's molecular binding interaction with metal clusters is essential to comprehending its mode of action and pharmacological effect [34]. Pyrazole and spiropyrazoline derivatives were chosen as template compounds because they are well-established bioactive scaffolds, widely reported to possess anticancer and kinase-inhibitory activity, including activity relevant to CDK targets. Their heterocyclic frameworks offer strong binding interactions, structural diversity, favorable drug-likeness, and excellent synthetic tunability, all of which make them highly suitable for molecular docking and rational drug design. Recent literature supports their use as promising lead structures in anticancer research [35,36]. Khaldan et al., reported an integrated computer aided methods to design potent glucosidase inhibitors based on bioactive derivatives [37]. A combined study of reverse docking, MD simulations, pharmacokinetics with DFT studies of garlic, triazole derivatives and trisubstituted thiazoles as an effective antifungal inhibitor was reported recently [38–40]. The development of more water-soluble alternative solid formulations could improve oral drug absorption. We have examined the interaction between the metal clusters in the anticancer drug PCB in light of these considerations.

The DFT technique can be used to calculate a molecule's chemical properties with high accuracy and at a low cost [41–46]. Recent years have seen the publication of numerous studies of metal clusters and therapeutic compounds [47–55]. In this work, a quantum computing technique is used to investigate various features of PCB adsorbed on Au_3 cluster. DFT techniques were applied to investigate the PCB-Au interaction mechanism.

2. Computational methods

The molecular structure, optical characteristics, and interactions of PCB with metal cluster for various configurations were analyzed using Gaussian16 at B3LYP/SDD level [56]. For optimal interaction, the PCB molecule is positioned in close proximity to the most reactive sites (PCB1, PCB2, PCB3 and PCB4 near to N6 atom of piperazine ring, N7 and N8 atoms, C22 =O2 and C16 =O1, respectively), maintaining a 3 Å spacing between them. In part, the core potential foundation was selected due to its capacity to do calculations more rapidly while preserving a somewhat greater degree of accuracy and structures [57]. FMOs and MEP analyses shed light on the structural characteristics and adsorption mechanism. Using Raman spectroscopy, the systems' adsorption behavior was investigated. The system was visualized using GaussView [58]. Since PCB is a medication used to treat breast cancer, molecular docking was used to shed light on the binding propensities of 5GS4 protein with the ligands PCB and PCB2-Au_3. The aim of this work is to shed light on the 5GS4 protein's binding preferences with the ligands PCB and PCB2-Au_3. In order to conduct docking studies on the molecules in issue, the PDB structure was first cleaned for their geometry by eliminating water and adducts using Autodock vs 4.2.6. Using the web-based P2RANK program, the binding sites for PCB and PCB2-Au_3 were identified [59]. After non-polar hydrogens were combined, both the target drug and the receptor were saved in pdbqt format. A grid box dimension for 22 × 50 × 39 Å was used for docking. Grid boxes with specific dimensions and 0.3 Å spacing have to be designed. The protein-ligand complex docking experiments were conducted using the Lamarckian Genetic Algorithm (LGA). Each of the three molecular docking inquiry replicates had 50 solutions, a population size of 500, 2500000 evaluations, a maximum generational number of 27, and all other parameters were set to their default levels. Following docking, the RMSD clustering maps were produced by re-clustering using the clustering tolerances of 0.25, 0.50, and 1 to identify the optimal cluster with the greatest number of populations and the lowest energy score.

5GS4 protein MD simulations, in conjunction with ligand PCB and PCB2-Au_3, were executed using vs 2020.1 Desmond simulation engine [60,61]. The simulations used a transparent model solvent with SPC molecules of water and were carried out at a physiological temperature of 37°C. The key elements of water-protein and water-ligand interactions, including as hydrogen bonding and electrostatic interactions, can be captured by the SPC water model. We have investigated the conformational changes, binding affinities, and dynamic behavior of the protein-ligand complex in a more realistic environment by solvating it with SPC water molecules. A 10 × 10 × 10 Å periodic boundary solvation box was used with the OPLS-2005 force field. Na+ ions were supplied to neutralize the system and a 0.15 M NaCl solution was added to replicate natural biological conditions. The OPLS_2005 force field is especially useful for researching the interactions between tiny molecules and the conformational behavior of proteins and nucleic acids [62]. In order to equilibrate the protein-ligand complexes, the system first went through a 10 ns stabilization phase in the NVT ensemble. After the, the NPT ensemble underwent a 12-ns equilibration and minimization. The Nose-Hoover chain coupling approach controlled the NPT ensemble by maintaining a temperature with relaxation durations set at 1.0 ps and a pressure control fixed at 1 bar during the run. For pressure control, the Martyna-Tuckerman-Klein chain coupling barostat method with a 2 ps relaxation period was used. While Coulomb interactions were limited to a 9 Å cut-off, long-range electrostatic interactions were calculated using the Ewald technique with particle mesh. The RESPA integrator with a time step of 2 fs was used to compute bonded forces for every trajectory. The simulation's production phase lasted for 100 nanoseconds in total. Several metrics, such as SASA, Rg, RMSF, and RMSD, were used to assess the system's stability during the simulation.

2.1. Binding free energy analysis

In this study, the binding affinities of ligand-protein complexes were analyzed using the Generalized Born Surface Area (MM-GBSA) technique, integrated with molecular mechanics. This method thoroughly evaluates binding free energies by considering molecular interactions and the impact of solvation. Binding free energy calculations via MM-GBSA were performed with the Python-based script which processed the final 50 frames from the simulation trajectory using a single-step sampling approach to enhance the precision of energy assessments. MM-GBSA computes binding free energy (ΔGbind) through an additive framework, accounting for various energetic factors.

The components contributing to the binding free energy included: **Electrostatic Interactions -** Forces between charged atoms within the system; **Hydrogen Bonding -** Stabilizing effects created when hydrogen atoms form bridges with electronegative atoms; **Van der Waals Forces -** Weak attractive forces occurring between nonpolar regions; **Covalent Bonding -** Strong bonds formed through shared electron pairs between atoms; **Intra-molecular Interactions -** Forces acting within the molecule itself; **Solvation Energy -** The energetic changes due to protein salvation; **Hydrophobic Effects -** Influences arising from the interaction between the ligand and non-polar regions; **Ligand-specific Energies -** Energetic properties intrinsic to the ligand itself.

ΔGbind= ΔGMM + ΔGsolv - ΔGSA and here's a breakdown of the terms: **ΔGbind**: The overall binding free energy of the ligand-protein complex; **ΔGMM**: The total molecular mechanics energy of the protein-ligand system in isolation, reflecting their inherent interactions without any external influences; **ΔGsolv**: This represents the difference in solvation energies, determined by subtracting the combined solvation energies of the unbound receptor and ligand from the solvation energy of the ligand-protein complex in its bound state; **ΔGSA**: The change in surface area energies between the ligand and the protein accounts for the surface area exposure changes upon binding. Understanding the interaction kinetics and stability of the ligand-protein complexes is made easier by this thorough study, which sheds light on how various chemical components affect the binding affinity of the complexes.

3. Results and discussion

3.1. Adsorption properties

The majority of the time, structural characteristics controls the interaction between PCB and metal cluster. The optimized PCB, Au_3 and PCB-Au_3 are shown in Fig. 1, S1 & Fig. 2.

In order to maximize interaction and likely find an adsorption site with metal clusters, PCB is first placed to the metal clusters, with a separation of less than 3 Å. This is based on the most reactive zones seen in the MEP of PCB (Fig. 1c). Bond length (Å) changes for PCB during adsorption are: C24-N5 (from 1.4844 to 1.4797), C24-C27 (from 1.5373 to 1.5369), C27-N6 (from 1.4728 to 1.5076) and C26-N6 (from 1.4728 to 1.5071) for PCB1; C25-N8 (from 1.3751 to 1.3612), C25-N4 (from 1.3449 to 1.3430), C25-N7 (from 1.3834 to 1.3984), C30-N8 (from 1.4212 to 1.4262) and C20-N7 (from 1.3400 to 1.3533) for PCB2; C22-O2 (from 1.2569 to 1.2825), C22-C29 (from 1.5190 to 1.5086) and C22-C18 (from 1.5090 to 1.4797) for PCB3 and C16-O1 (from 1.2640 to 1.2860), C16-N3 (from 1.4187 to 1.3982) and C16-C18 (from 1.4771 to 1.4589) for PCB4. Importantly, the bond length data show significant variation following addition of Au_3, showing that PCB is adsorbed on metal cluster. In the case of PCB1/3/4 complexes, Au atom is at a distance of 2.1982 from N6, 2.1788 from O2 and 2.2026 Å from O1, respectively, while for PCB2, N7 atom is bonded to Au with a bond length of 2.1375 Å. All modifications to PCB's structural characteristics are linked to the charge transfer between metal and PCB [63]. The adsorption energy $E_a = E_c - E_{PCB} - E_m$ where E_c, E_{PCB}, and E_m are energies of the PCB-Au_3 cluster, PCB, and Au_3 [42,43] and E_a are −28.64, −31.40, −19.77 and −16.86 kcal mol^{-1} in vacuum for PCB1/2/3/4 with Au_3 cluster (Table 1). The configuration PCB2 gives highest adsorption energy. The complexes are simulated at geometric gCP, which can treat both inter- and intra-molecular BSSE [64,65]. The B3LYP-gCP-D3/SDD energy corrections are also made from Gimme's web service [66–68] and the obtained adsorption energy after BSSE correction is −27.82/-30.68/-18.12/-14.97 kcal mol^{-1} in air and −39.55/-50.27/-35.78/-34.13 kcal mol^{-1} in water, for PCB1 to PCB4 complexes.

3.2. Chemical properties

MEP is one method for looking the reactive sites [69]. The charge density and reactive site can be found using the potential surface of carious colors red/blue/green (electrophilic/nucleophilic/neutral), which indicates the negative/positive/zero potential, respectively. For PCB, electrophilic sites are seen at nitrogen and oxygen (Fig. 1). The hydrogen atoms are surrounded by a positive electric potential. Following adsorption, there was a positive potential in Au_3 and a negative potential on the O and N atoms due to the potential's redistribution (Fig. 3). Potential changes show that charge is transferred between metal and PCB during the adsorption process [70].

From the IR spectrum (Figure S2) the important functional groups are: 3244, 3169, 1560,685 (NH), 3010, 2924, 1426, 1205, 1037, 962 (CH3), 2852, 1451, 907, 832, 812 (CH2), 1592 (C═O), 1401, 1265, 1243 (CN), 1152 (CH), 1072 cm^{-1} (CC) and at 3486, 3417, 1553, 676 (NH), 3009, 2922, 1423, 1208, 1036, 954 (CH3), 2879, 1450, 908, 833, 814 (CH2), 1588 (C═O), 1403, 1269, 1242 (CN), 1151 (CH), 1084 cm^{-1} (CC) theoretically [71–73].

TD-DFT is used to model UV-Vis spectra for PCB and PCB-Au_3. Figures S3 to S5 (PCB, PCB-Au_3 in vacuum and water) give peaks for PCB (227, 273, 281 and 359 nm as experimental with DFT values 334 and 415 nm), while that of PCB-Au_3 are at higher values (Table S1) [74]. For PCB-Au_3, one peak is seen in the visible region at 625 (PCB3) and 653 (PCB4) for Au_3 cluster systems in vacuum, while in aqueous medium it is at 592 (PCB4). Higher oscillatory power and a high energy transition have been attributed to these theorized peaks [75]. Shift to higher value results from surface Plasmon resonance shifting to lower energies when Au is adsorbed on PCB. The red shift figures show how the system size grows [76–79]. The observed red-shift in the TDDFT-calculated excitation is consistent with the well-known tendency of B3LYP to underestimate excitation energies for transitions with long-range or partial charge-transfer character, confirmed by our orbital analysis; tests with larger basis sets show that the functional, rather than the basis, is responsible for this deviation. While long-range-corrected functionals can improve quantitative accuracy, their substantially higher computational cost for this system and the need for methodological consistency with prior studies justified our use of B3LYP/SDD; nevertheless, we now include a CAM-B3LYP calculation in the Supporting Information, which reproduces the expected shift and supports our explanation (Figure S6).

The FMOs study provides information on the kinetic stability and reactivity of the system [80]. The system's chemical reactivity is revealed by the energy differential. A soft molecule is one that has a small energy gap (Eg), high polarizability, and high reactivity [81]. HOMO of PCB are over the piperzine and pyridine rings mainly and O2 atom (Fig. 1) while the LUMO is over the other rings, in addition to C═O groups. The HOMOs are also localized over the N4-N7 ring and Au_3 for PCB1; N4-N7 ring, N9 ring, C═O groups and Au_3 for PCB2; N9 atom ring and Au_3 for PCB3 and PCB4 and LUMO is over N4-N7 and N3 rings without over N3 atom for PCB1; N9 atom ring, C22 =O2 and Au_3 for PCB2; N9 ring and Au_3 for PCB3 and PCB4 (Fig. 4).

The shifting of MOs indicates the mechanism of charge transfer (CT) from the metal clusters to PCB [72,82]. The Eg vlaues of PCB- Au_3 clusters (2.0297, 1.9635, 1.2337 and 1.4114 eV for PCB1 to PCB4) are less than that of PCB (3.3372 eV) in vacuum (Table 2). Generally speaking, the energy gap helps determine the CT and NLO characteristics; a lower Eg denotes a more reactive system [52]. The NLO activity is enhanced by PCB-adsorbed metal clusters' increase polarizability, as seen by the decrease in the Eg from 3.3372 eV of PCB following adsorption. Adsorption process's lowering of energy gap values is supported by the DOS spectra (Figure S7a & S7b). Higher polarizability values are frequently linked to more active NLO characteristics. After

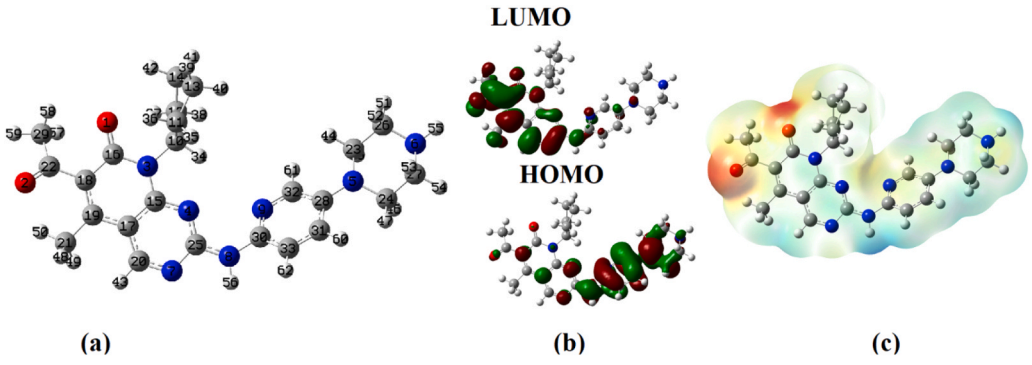

Fig. 1. PCB's (a) optimized geometry (b) FMOs (c) MEP plots.

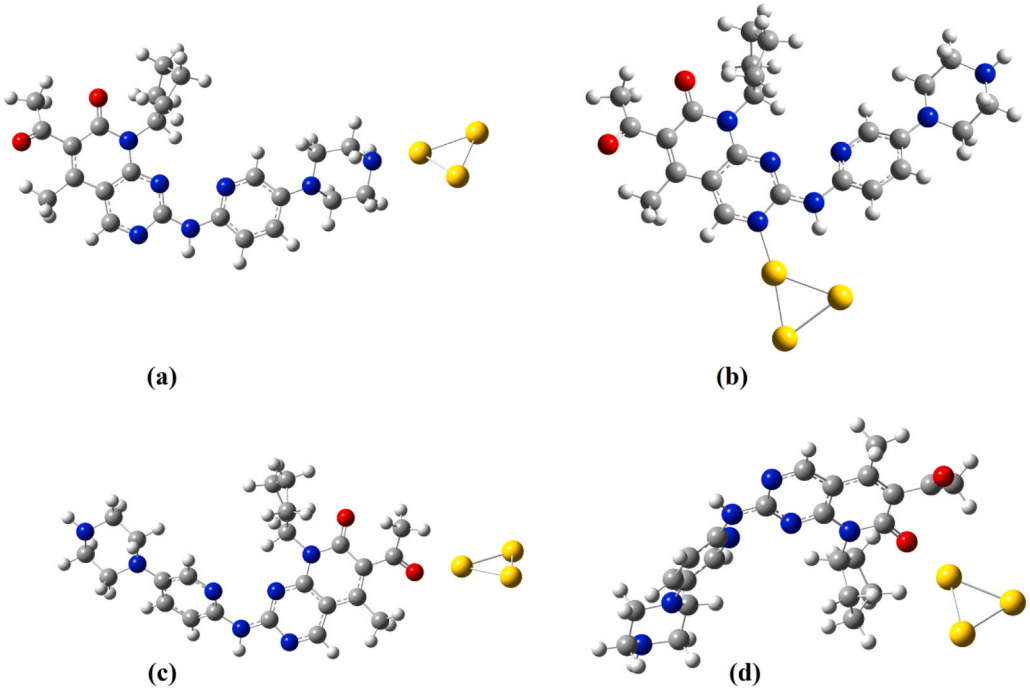

Fig. 2. Optimized geometries of (a) PCB1 (b) PCB2 (c) PCB3 (d) PCB4.

Table 1
Energies, dipole moments, polarizability and adsorption energies.

Systems	Energies (a.u.)	Dipole moments (Debye)	Polarizability (a.u.)	Adsorption energy (kcal mol^{-1})	E_{gCP-D3} (kcal mol^{-1})
PCB	-1465.498 471	9.3785	345.4333		-
Au_3	-407.367 901	0.3372	139.841		-
Vacuum					
PCB1	-1872.912 017	7.1839	405.46	-28.64	-27.82
PCB2	-1872.916 412	7.9355	496.991	-31.40	-30.68
PCB3	-1872.897 874	17.6689	605.1953	-19.77	-18.12
PCB4	-1872.893 240	15.1592	502.857	-16.86	-14.97
Water					
PCB1	-1872.931184	11.2967	818.9537	-41.08	-39.55
PCB2	-1872.947645	7.6683	834.8053	-51.00	-50.27
PCB3	-1872.925207	21.8218	1117.9243	-36.92	-35.78
PCB4	-1872.923424	17.4195	752.255	-35.80	-34.13

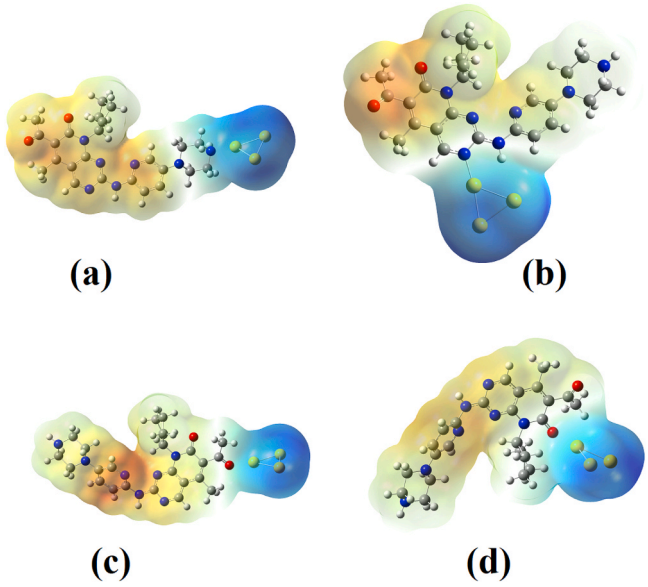

Fig. 3. MEP plots of (a) PCB1 (b) PCB2 (c) PCB3 (d) PCB4.

adsorption on metal clusters, PCB exhibits increased polarizability (Table 1) [83]. To observe the effect of a higher functional, the chemical descriptors of the complex having highest adsorption energy is calculated using PBE0 functional and the values are: EH = -5.9130/-4.6729/-4.2479 eV; EL= -3.9279/-2/6626/-3/2637 eV; Eg = 1.9851/2.0103/0.9842 eV; Hardness = 0.9926/1.0052/0.4921 eV; chemical potential = -4.9205/-3.6678/-3.7558 eV and electrophilicity index = 12.1959/6.6916/14.3325 eV, for Au_3/PCB/PCB2 systems, respectively and for PCB2 complex, the adsorption energy was found as −41.13 kcal mol^{-1} [84].

In PCB adsorption with metal clusters, the O1 (-0.30) and O2 (-0.27) atom's charge (obtained from NBO analysis) becomes −0.28, −0.29 and −0.40 for PCB2 to PCB4 and −0.26, −0.26, −0.37 and −0.25 for PCB1 to PCB4 (Table S2). Similarly, the charge of N4 (-0.05) becomes −0.02 for PCB1 and −0.04 for PCB3 and PCB4 and that of N5 (-0.22) and N6 (-0.32) becomes −0.20 and −0.49 for PCB1 without any change for other complexes. N7 (-0.08) and N8 (-0.40) of PCB becomes −0.09, −0.37 for PCB1, −0.37 and −0.44 for PCB2, −0.07 and −0.40 for PCB3 and PCB4. PCB's C11 (-0.44) becomes −0.72 for PCB4 and C16 (0.11) becomes 0.09 and 0.23 for PCB2 and PCB4. PCB's C17 (0.17) becomes 0.15 and 0.16 for PCB2 and PCB3. PCB's C18 (-0.08) becomes −0.07, −0.05 and 0.00 for PCB2 to PCB4. For PCB3, C22 has a charge value of 0.31 while that of PCB is 0.15. For PCB1, C23and C24 has a charge value of −0.37 while that of PCB is −0.29 and also C27 value becomes −0.28 with pristine charge as −0.36. The hydrogen atoms are all positively charged. Based on the Mulliken charge on the PCB after adsorption over the Au_3, for the complexes, the charge values are 0.32, 0.23, 0.27 and 1.97 for PCB1 to PCB4 and a positive sign indicates that the charge is transferred from PCB to Au_3 [85]. Strong interaction and charge transfer

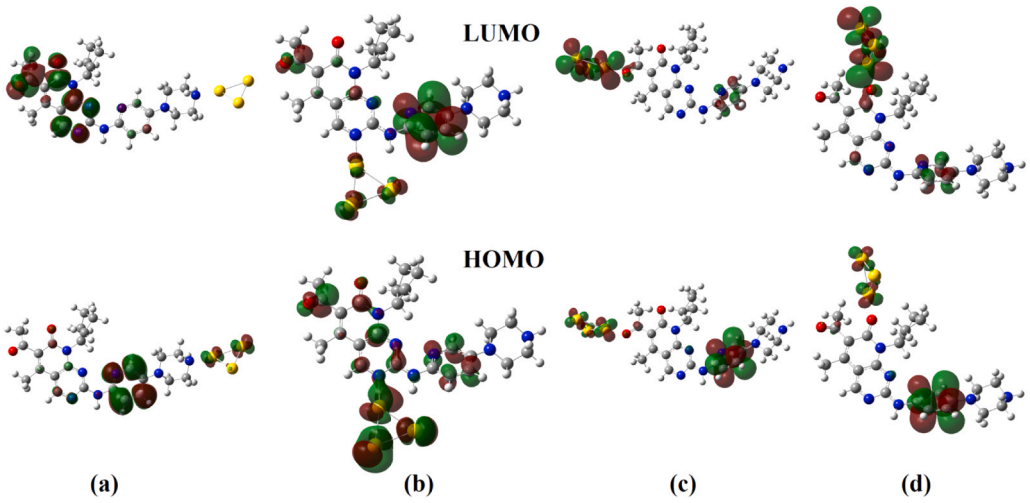

Fig. 4. FMOs plots of (a) PCB1 (b) PCB2 (c) PCB3 (d) PCB4.

Table 2
Chemical descriptors (eV).

Systems	EH	EL	Eg	Hardness	Chemical potential	Electrophilicity index
PCB	-5.4678	-2.1306	3.3372	1.6686	-3.7992	4.3252
Au_3	-6.3785	-3.3739	3.0046	1.5023	-4.8762	7.0136
Vacuum						
PCB1	-4.4583	-2.4286	2.0297	1.0149	-3.4435	5.8416
PCB2	-4.6919	-2.7284	1.9635	0.9818	-3.7102	7.0102
PCB3	-4.1910	-2.9573	1.2337	0.6169	-3.5742	10.3538
PCB4	-4.1592	-2.7478	1.4114	0.7057	-3.4535	8.4502
Water						
PCB1	-4.1334	-2.7823	1.3511	0.6756	-3.4579	8.8490
PCB2	-4.2653	-3.0283	1.2370	0.6185	-3.6468	10.7511
PCB3	-4.1437	-3.3410	0.8027	0.4014	-3.7424	17.4454
PCB4	-4.6038	-2.5989	2.0049	1.0025	-3.3044	5.4458

are connected; hence, a strong interaction will occur when the charge transfer between the adsorbents and adsorbates is higher, and vice versa [86]. According to Table S3, the process is exothermic and spontaneous since all of the changes in thermo dynamical values for PCB and PCB-Au_3 are negative.

3.3. SERS analysis

Raman spectra were examined to gain a better understanding of PCB adsorption on metal clusters (Figure S8 for PCB and Figures S9 to S12 for PCB1 to PCB4). According to the Raman intensity values, some of the PCB peaks had grown allowing adsorption on the metal clusters. The peaks in the PCB-adsorbed metal clusters below 300 cm^{-1} are caused by the interaction between metals and PCB. The υNH mode of PCB at 3486 and 3417 cm^{-1} is red shifted to 3479, 3323 (PCB1), 3420, 3293 (PCB2), 3487, 3420 cm^{-1} (PCB4) due to adsorption with Au_3. It demonstrates how the NH group allows PCB to be adsorbed with Au_3. The red shift of PCB's δNH at 1553, 676, 592 cm^{-1} becomes 1530, 663 (PCB1), 1458, 618 (PCB2), 1492 (absent in PCB) 672 (PCB3), and 1543, 663 cm^{-1} (PCB4) after adsorption with Au_3. The υCH3 mode of PCB at 3009, 2922 cm^{-1} are shifted to 3025, 2937 (PCB1), 3015, 2937 (PCB2), 3008, 2931 cm^{-1} (PCB4) due to the adsorption with Au_3 cluster. The δCH3 modes of PCB at 1423, 1208, 1036, 954 cm^{-1} are shifted to 1422, 1223, 1026 (PCB1), 1387, 1228, 1035, 965 (PCB2), 1431, 1223, 1026, 952 (PCB3) and 1239, 1028 cm^{-1} (PCB4). The υCH2 of PCB at 2879 cm^{-1} is shifted to 2891 (PCB2), 2889 cm^{-1} (PCB4) due to the adsorption with Au_3 cluster. The δCH3 modes of PCB at 1450, 908, 833, 814 cm^{-1} are shifted to 1464 (PCB1), 1457 (PCB2), 1460, (PCB3) and 1475, 933, 842,815 cm^{-1} (PCB4). The υC═O of PCB at 1588 cm^{-1} is shifted to 1586 (PCB1), 1555 (PCB2), 1567 (PCB3), 1576 cm^{-1} (PCB4) due to the adsorption with Au_3 cluster. The CN stretching mode of PCB at 1403, 1269, 1242 cm^{-1} is shifted to 1391, 1244, (PCB1), 1401, 1253, 1225 (PCB2), 1399, 1276, 1239 (PCB3), 13390, 1271, 1244 cm^{-1} (PCB4).

Also, a number of modes which are absent in PCB appear in PCB-metal clusters after adsorption. Based on the Raman intensity values, SERS effect also causes an rise in intensity in certain PCB-metals system frequencies via the N6, N7, O2 and O1 for the configurations, PCB1, PCB2, PCB3 and PCB4 due to the shifts in wavenumbers and changes in Raman intensity, which suggest a tilted orientation for PCB [87–89].

3.4. Solvent effect

Because solubility can limit or expand the usage of materials, it is beneficial in a variety of areas [90–93]. To model aqueous effects we used CPCM with water (ε = 78.4) and the default UFF radii (Gaussian implementation), using identical electronic-structure settings. Since the solvation energies (SEs) for PCB1/2/3/4 are −41.08/-51.00/-36.92/-35.80 kcal mol^{-1}, PCB-Au_3 is stable in an aqueous media (Table 1) [55]. With the exception of PCB2, the PCB-Au_3 clusters DM increased in the water phase (Table 1). Increase in DM in water confirms that PCB delivery demonstrating its superior drug deliver properties [94]. According to Table S3, the process is exothermic and spontaneous since all of the changes in thermo dynamical values for PCB and PCB-Au_3 clusters are negative. In gaseous medium, PCB-metal clusters - aside from PCB4 water-have the largest change in Gibbs energy. Gibbs energy and enthalpy changes are increasing in aqueous fluids relative to gaseous media [95].

3.5. Reactivity analysis

In multiwave function analysis [96], the Electron Localization Function (ELF) [97] is a useful indicator for comparing electron pairing and localization among computational techniques. By superimposing ELF on wavefunctions derived from Hartree-Fock, DFT, and correlated techniques, one can evaluate method-dependent changes in bonding descriptions. This comparison technique allows for a more thorough assessment of whether electron localization is maintained or altered at various theoretical levels. ELF is thus a chemically comprehensible benchmark against which to validate electronic structure predictions in a range of quantum chemical theories.

Different electronic characteristics between PCB and PCB-Au_3 are revealed by the ELF analysis, emphasizing the effect of functional substitution on electron distribution. High electron localization (ELF ≈ 0.85–0.90) is uniformly seen along the conjugated core in the PCB's ELF-colored map (Figure S13a), suggesting strong covalent character and extended π-delocalization. Bonding uniformity and delocalized electron density are further confirmed by the symmetrical and closely clustered contours surrounding the C-C bonds in the aromatic ring in the corresponding contour plot (Figure S13b). However, the PCB-Au_3 ELF-colored map (Figure S14a) shows changed localization close to the Au substituent, where ELF values drop to roughly 0.72–0.78, indicating electron density distortion that is probably caused by the substituent's steric influence or electron-withdrawing effects. Furthermore, areas around heteroatoms in the Au fragment show increased ELF values over 0.90, assigned to localized lone pair electrons. Figure S14b confirms these variations by showing distortion and elongation of valence basins close to the replacement site on the ELF-contour plot of PCB-Au as opposed to the symmetric pattern observed in PCB. Both systems maintain significant core localization (ELF > 0.98) around inner atomic areas, indicating little disturbance to core electronic structure. These results taken together imply that the Au moiety in PCB-Au disturbs electronic symmetry and creates localized polarization, therefore possibly increasing chemical reactivity, changing donor-acceptor behavior, and changing non-covalent interaction potential relevant for functional material and supramolecular uses.

The Localized Orbital Locator (LOL) (based on kinetic energy density) complements ELF in multi wavefunction studies by emphasizing localized orbital properties [98]. When applied to wavefunctions from various electronic structure approaches, LOL facilitates in the finding of tiny orbital localization and bonding character changes. Its responsiveness to kinetic distribution adds another level to which electronic properties can be compared across theories. LOL is thus useful in understanding bonding details and verifying electronic explanations in multi-method investigations [99]. The LOL analysis provides a thorough view on electron localization in molecular systems. Especially in the aromatic framework, the LOL contour (Figure S15a) and colored map (Figure S15b) for the compound PCB show well-defined areas of high localization (LOL > 0.8) along the σ-bonds. Indicating strong covalent character and minimal electron delocalization, these areas show as dense contours and intense red patches. The LOL diagrams for PCB-Au (Figure S15c and S15d), on the other hand, show a more widespread distribution of electron density. With LOL values between 0.3 and 0.6 around the Au-substituted segment, the contour lines are more disperse and the colored plot indicates notable green to light blue regions. This implies partial delocalization, probably caused by π-conjugation or electron-donating influences generated by the Au moiety. The observed delocalization in PCB-Au suggests a redistribution of electron density over extended molecular orbitals, which could lower the HOMO-LUMO energy gap and enhance electronic interaction throughout the structure. Therefore, although PCB keeps a mostly localized electronic character, PCB-Au shows notable electronic delocalization, a difference with possible consequences for its optical behavior and chemical reactivity.

Assessing weak intermolecular forces is essential for determining the stability, reactivity, and supramolecular assembly of molecules. The Reduced Density Gradient (RDG) approach [100], paired with Density Functional Theory (DFT), is a popular visualization technique for finding and describing non-covalent interactions. RDG plots use electron density and gradient to identify favorable hydrogen bonding, π-π interactions, and repulsive steric forces. In the present work, RDG analysis was carried out using a multiwavefunctional DFT model to investigate and compare the non-covalent interaction. In Figure S16a, the RDG scatter diagram for PCB displays a typical symmetric profile around the origin, with dominating spikes in the low-gradient zone at near-zero $\lambda_2\rho$ values. This implies that the molecule is mostly influenced by weak van der Waals forces. In Figure S16b, the isosurface plot is shown. It shows diffuse green surfaces over the molecular backbone, emphasizing the importance of dispersion interactions and the absence of significant electrostatic or hydrogen bonding interactions. On the other hand, the RDG profile of PCB-Au shows a more abundant and diverse interaction environment. In Figure S16c, the RDG scatter plot shows more prominent spikes pointing into the negative $\lambda_2\rho$ area, indicating strong attractive interactions, particularly hydrogen bonding and π-π stacking effects. The related isosurface diagram in Figure S16d displays blue patches near the Au-substituted regions, which indicate greater electron delocalization and the appearance of specified, stabilizing forces. The presence of red patches also indicates steric repulsion, particularly near the big Au group, which contributes to the molecule's overall conformational rigidity.

This comparative RDG analysis clearly demonstrates the impact of Au functionalization on the parent PCB structure's electrical and interaction profiles. The Au substitution not only enhances electron-rich areas, but it also introduces a balance of attractive and repulsive interactions, which may alter molecule stability as well as its potential utility in supramolecular applications or sensor design.

3.6. Sensor properties

Recovery of a sensor is crucial and can be accomplished by either heating it to a higher temperature or exposing to light [101]. The recovery time, $\tau = \upsilon^{-1} \exp(-E_a/kT)$ [102,103]. In contrast to the weaker metal-drug interaction, which promotes rapid reversibility, the stronger metal-drug interaction causes slower desorption and prolonged recovery, which is consistent with its higher binding energy and charge transfer. According to these findings, the metal-based devices provide the best balance between recovery rate and sensitivity for sensing applications. For instance, ΔEg aids in determining the drug's presence and how it adheres to the clusters [50]. The drug can be identified by generating an electrical pulse, which will cause the conductivity to increase due to the decrease in Eg. As a result, the findings show that the drug may be identified by the sensor using the metal moieties. A process called desorption can occur when a drug is exposed to light. A higher temperature should be used to speed up the desorption process or shorten recovery times. Actually, at 400 K, drug recovery from metal surface happens rapidly (Table 3). Therefore, Au_3 could be a good choice for developing small sensors for drug-specific detections. The drug's

Table 3
Recovery time (second) for the recovery of PCB from the metal surfaces at 400 K.

Complex	Binding energy (kcal/mol)	Attempt frequency (Hz)		
		3.0×10^{16}	7.5×1014	4.3×1010
Vacuum				
PCB1	-27.82	5.29E-02	2.12E+ 00	3.69E+ 04
PCB2	-30.68	1.93E+ 00	7.73E+ 01	1.35E+ 06
PCB3	-18.12	2.65E-07	1.06E-05	1.85E-01
PCB4	-14.97	5.04E-09	2.02E-07	3.51E-03
Water				
PCB1	-39.55	1.36E+ 05	5.43E+ 06	9.46E+ 10
PCB2	-50.27	9.76E+ 10	3.91E+ 12	6.81E+ 16
PCB3	-35.78	1.18E+ 03	4.73E+ 04	8.24E+ 08
PCB4	-34.13	1.48E+ 02	5.93E+ 03	1.03E+ 08

recovery time from Au_3 surface will be calculated using different try frequency. These results indicate that most Au_3-PCB systems benefit from a litter recovery period.

3.7. Docking and MD simulations

The docking result presented in the image illustrates (Figure S17a) the binding mode of PCB within the active site of the 5GS4, with a predicted binding energy (BE) of -8.6 kcal mol^{-1} indicates a moderately strong and thermodynamically favorable interaction. Based on methodological and structural factors, PDB, 5GS4 was selected as the receptor structure for docking studies. 5GS4 is the ligand-binding domain of the human estrogen receptor-α (ERα), a protein that is essential to the biology of hormone-driven breast cancer, even though palbociclib is traditionally known to target CDK4/6. We want to determine whether palbociclib had any potential for off-target or auxiliary interactions with ERα that could contribute to its biological activity of therapeutic synergy because it is clinically utilized in conjunction with endocrine therapy for ER-positive breast cancer.

The left side of the image shows the 3D protein-ligand complex where PCB, colored in red, is positioned snugly within the binding pocket formed by several hydrophobic and aromatic residues, visualized within a semi-transparent surface and ribbon structure. On the right, a detailed 2D interaction diagram provides a comprehensive view of the specific residues engaged in different non-covalent interactions stabilizing the complex. Key van der Waals interactions are observed with residues like LEU402, LEU391, MET388, LEU387, and LEU384, contributing to the overall hydrophobic environment of the binding cavity that favors the lipophilic character of PCB. Additionally, alkyl and pi-alkyl interactions involving LEU428, MET388, MET343, VAL347, and LEU350 further stabilize the ligand through dispersive forces, enhancing binding affinity. Notably, π–π stacking interactions are in aromatic rings of the ligand and residues such as PHE404, PHE425, and TRP438, which play a critical role in anchoring the planar moiety of PCB, a crucial determinant in drug-like molecules targeting hydrophobic cavities. Carbon-hydrogen bonds, albeit weaker, contribute to specificity and additional stabilization through interactions with nearby residues. Furthermore, residues such as HIS524, LYS529, and ALA544, although not directly forming strong bonds, are spatially positioned to modulate the local environment and potentially participate in dynamic hydrogen bonding or electrostatic interactions during molecular dynamics simulations. Collectively, this diverse array of non-covalent interactions underscores the ligand's complementary fit and favorable energetic profile within the 5GS4 binding pocket, offering valuable insights for structure-based optimization of PCB analogs with improved binding affinity and pharmacological potential.

The docking interaction analysis between the 5GS4 protein and the PCB2 ligand, presented with a BE of -8.4 kcal mol^{-1}, reveals a well-stabilized and multifaceted binding environment within the receptor's active pocket. The 3D and 2D interaction diagrams demonstrate that the PCB2 ligand is firmly accommodated within the hydrophobic core of 5GS4, engaging in diverse non-covalent interactions that collectively stabilize the complex (Figure S17b). The ligand is primarily stabilized by several hydrophobic alkyl and pi-alkyl interactions involving residues such as MET A:388, LEU A:387, ALA A:350, and LEU A:346. These interactions contribute to the snug fitting of the ligand's aromatic and non-polar moieties within the receptor's hydrophobic cleft. Notably, van der Waals forces, represented by residues like LEU A:428, MET A:522, and GLY A:420, play a significant role in complementing the binding through close, non-specific contacts that enhance packing efficiency. Conventional hydrogen bonds formed by MET A:421 and carbon-hydrogen bonds involving GLY A:421 further augment the binding specificity by providing directional stabilization. Additionally, pi–lone pair interactions with GLU A:353 highlight electronic complementarity, while pi–alkyl interactions with residues like PHE A:404 and PHE A:425 further anchor the ligand's aromatic systems. Interestingly, the presence of an Au cluster attached to the ligand structure likely influences binding affinity by influencing the electronic density distribution of the ligand, thereby modulating its interaction with the surrounding polarizable amino acid side chains. The Au cluster may also promote pi-metal coordination-like interactions or stabilize aromatic stacking, indirectly strengthening van der Waals contacts or polar interactions. The combined effect of hydrophobic, hydrogen bonding, and possible metallophilic contributions from the Au cluster underscores the ligand's improved binding profile and highlights the multifactorial nature of effective molecular recognition in this protein-ligand system.

PCB and PCB2 show comparable binding energies, but the nature of their stabilization differs. PCB primarily relies on strong π–π stacking (PHE404, PHE425, and TRP438) and dense hydrophobic packing deep inside the pocket. In contrast, PCB2-due to the presence of a gold cluster—shifts toward π–alkyl, hydrogen bonding (MET421), π–lone pair interactions (GLU353), and enhanced electronic complementarity, resulting in a more diverse but slightly less π-stack-dependent mode of interaction. The Au cluster likely increases ligand polarizability, allowing new interaction modes not observed in PCB (Table 4).

The superimposition analysis of the three structural overlays -5GS4–PCB vs. native 5GS4, 5GS4–PCB2 vs. native 5GS4, and 5GS4–PCB vs. 5GS4–PCB2 reveals minimal conformational deviations, reflected by RMSD values of 0.353 Å, 0.240 Å, and 0.184 Å, respectively, indicating that ligand binding induces only subtle local adjustments without disturbing the global fold of 5GS4. In the first comparison, the slightly higher RMSD (0.353 Å) suggests that PCB binding produces minor rearrangements primarily around the active-site helices and loop regions, yet the overall α-helical architecture remains intact. The second overlay, involving PCB2, shows an even lower deviation (0.240 Å), implying that the Au-conjugated ligand fits more snugly into the pocket with minimal structural perturbation, likely due to enhanced electronic complementarity and tighter packing interactions. The third comparison between the PCB- and PCB2-bound structures exhibits the smallest RMSD (0.184 Å), reflecting that both ligands occupy nearly identical spatial orientations and induce comparable micro-adjustments in surrounding residues. Collectively, the very low RMSD values across all overlays confirm that both ligands bind stably within the catalytic pocket while preserving the native conformation of 5GS4, and the Au cluster subtly refines rather than disrupts structural alignment. Figure S18 gives the superimposition of 5GS4 with 5GS4–PCB, 5GS4 with 5GS4–PCB2 and 5GS4–PCB with 5GS4–PCB2 illustrating structural alignment and conformational stability upon ligand binding.

The provided graph illustrates the RMSD (100 ns) MD simulation for two protein-ligand complexes: 5GS4_PCB and 5GS4_PCB2, presumably representing the 5GS4 protein bound to ligand PCB alone and the PCB2 complex, respectively (Fig. 5a). RMSD is a critical term in MD simulations used to assess the structural stability of bio-molecular systems by measuring the average deviation of a protein's atomic positions over time relative to a reference structure, typically the initial conformation. In this plot, both systems display an initial rapid rise in RMSD within the first 5 ns, which is expected as the complexes adjust to simulation conditions. Subsequently, the 5GS4_PCB complex (red line) stabilizes at an RMSD value around 2.0 Å, whereas the 5GS4_PCB2 complex (black line) fluctuates more, settling near 2.5–3.0 Å. These observations indicate that the 5GS4_PCB complex maintains higher structural stability throughout the simulation compared to the 5GS4_PCB2 complex, which exhibits greater conformational flexibility or possible destabilization due to the binding of the PCB2 adduct. A generally accepted threshold for a well-behaved protein system in MD simulations is RMSD stabilization below 3.0 Å [104].

The fact that both complexes remain under this threshold suggests acceptable simulation quality, though the lower RMSD of 5GS4_PCB signifies a comparatively more stable binding interaction with the PCB ligand alone. The increased fluctuations in the 5GS4_PCB2 complex could stem from steric hindrance or altered electrostatic interactions introduced by the Au moiety, potentially disrupting native contacts

Table 4
Quantitative comparison of the key modulator interactions formed by ligands PCB and PCB2 within the active site of the 5GS4 protein.

Interaction Feature	PCB-5GS4 complex	PCB2-5GS4 complex	Comparative insight
Binding energy	-8.6 kcal mol^{-1}	-8.4 kcal mol^{-1}	Nearly identical affinity: PCB slightly stronger by 0.2 kcal mol^{-1} (not significant)
Primary stabilizing forces	Hydrophobic + π-π stacking dominant	Hydrophobic + π-alkyl + metallophilic effects	Both rely heavily on hydrophobic packing; PCB2 gains electronic modulation through Au cluster
van der Waals contacts	LEU402, LEU391, MET388, LEU387, LEU384	LEU428, MET522, GLY420	PCB forms vdw contacts deeper in the pocket; PCB2 shifts interactions toward more surface-proximal residues.
Hydrophobic (Alkyl/Pi-Alkyl) interactions	LEU428, MET388, MET343, VAL347, LEU350	MET388, LEU387, ALA350, LEU346	PCB2 shows more compact alkyl interactions around residue cluster 346–388 region.
Aromatic interactions (π-π/π-alkyl)	PHE404, PHE425, TRP438 (strong π–π stacking)	PHE404, PHE425 (π–alkyl; reduced π–π)	PCB shows stronger classical π–π stacking; Au conjugation shifts PCB2 toward π–alkyl and lone-pair interactions.
Hydrogen bonding	Weak C-H bonds with nearby residues	Conventional H-bond: MET431; C-H bond: GLY421	PCB2 forms stronger, defined hydrogen bonding, improving specificity.
Other electronic interactions	No significant observation	π–lone pair interaction with GLU353	Unique to PCB2; indicates enhanced electronic complementarity due to Au cluster.
Influence of Au cluster	No significant observation	Enhances polarizability; may support π–metal and metallophilic interactions	Distinguishing feature: PCB2 gains stabilizing electronic effects absent in PCB.
Nearby but Non-bonded modulating residues	HIS524, LYS529, ALA544	Not applicable	PCB interacts with more distal residues that may influence MD behavior.
Overall binding character	Strong aromatic anchoring + hydrophobic pocket fit	Multi-factor stabilization: hydrophobic + H-bond + Ag-mediated electronic tuning	PCB anchors deeper via π–π stacking; PCB2 relies on diverse interactions boosted by metal presence.

within the binding pocket. This pattern aligns with findings by Hollingsworth and Dror [105], who emphasized that ligand modifications often impact protein flexibility and stability, observable through RMSD analysis.

In MD simulations, RMSF is an essential statistic that assesses the mobility and flexibility of individual residues within a protein structure throughout the simulation (Fig. 5b). It provides residue-wise insights by calculating the average deviation of a particular residue from its mean position throughout the trajectory, with higher RMSF values typically indicating greater flexibility and lower values suggesting rigidity and stability. In the provided RMSF plot, the residue indices of the protein structure 5GS4 bound to two different ligands, PCB (red) and PCB2 (black line), are compared. Notably, both profiles exhibit similar fluctuation patterns with marked peaks and troughs across specific residue regions, reflecting consistent structural motifs within the protein. However, certain differences in amplitude suggest ligand-induced modulation of flexibility. The most prominent peak is observed around residue index 35 for both complexes, though the amplitude is significantly higher for the 5GS4_PCB2 complex, indicating a local region of enhanced flexibility upon binding with PCB2. Additionally, secondary peaks around residue indices 150 and 200 also show higher fluctuations for 5GS4_PCB2 compared to 5GS4_PCB, implying that PCB2 binding induces overall increased mobility in certain regions of the protein (Fig. 5b). This suggests that while the overall structural framework of 5GS4 remains conserved, ligand binding subtly affects local flexibility profiles, which may have implications for protein function and ligand-induced conformational dynamics. The overall RMSF values for both complexes largely remain within the acceptable range (0.5–3 Å) across most residues, barring specific flexible loops, indicating a good quality simulation without unrealistic atomic displacements [106]. The RMSF profile thus reflects a balanced simulation where structural integrity is preserved while capturing functionally relevant dynamic motions, supporting its reliability and interpretive value for studying protein-ligand interactions [107].

The Rg is a parameter in MD simulations that measures the distribution of a protein's atoms relative to its center of mass, providing insight into the protein's overall compactness and folding behavior throughout a simulation. Lower Rg values generally signify a more compact and tightly folded structure, while higher values indicate structural expansion or partial unfolding. In the presented Rg plot, the temporal evolution of the 5GS4 protein complexed with two ligands, PCB (red) and PCB2 (black), is checked over a 100 ns simulation timeframe. Average Rg for both complexes fluctuate within a narrow range of approximately 18.1–18.6 Å (Fig. 5c), suggesting overall structural stability without drastic unfolding events. The 5GS4_PCB2 complex demonstrates a slightly lower average Rg than the 5GS4_PCB2 complex during most of the simulation, implying that binding of PCB2 may confer marginally greater compactness to the protein compared to PCB. Notably, transient fluctuations are observed in both systems, which are typical in MD simulations and reflect natural protein breathing motions. Around the 60 ns mark, both complexes exhibit a brief convergence toward lower Rg values, suggesting transient compaction, before returning to their respective baseline averages (Fig. 5c). The absence of sustained high Rg values and the maintenance of Rg within a narrow, biologically plausible range throughout the simulation indicates a high-quality, well-equilibrated simulation without artifacts such as protein denaturation or unnatural expansion. This behavior aligns with findings from comparable protein-ligand MD studies, where minimal Rg fluctuation is considered indicative of simulation reliability and protein structural integrity [108]. Overall, these results suggest that both ligands sustain the folded state of 5GS4, with PCB2 marginally promoting a more compact and potentially stable conformational ensemble [109].

Hydrogen bonding is a pivotal non-covalent interaction that contributes significantly to the stability and specificity of protein-ligand complexes in molecular dynamics (MD) simulations. It provides valuable insight into the strength and consistency of molecular interactions over time. In the presented hydrogen bond plot for the 5GS4 protein bound to ligands PCB (red line) and PCB2 (black line), the number of hydrogen bonds is monitored across a 100 ns simulation period (Fig. 5d). Both complexes predominantly maintain between zero and one hydrogen bond throughout the trajectory, with occasional transient increases to two in the 5GS4_PCB2 system, particularly after the 70 ns mark. This suggests that while the interaction interface between the protein and both ligands involves intermittent hydrogen bonding, it remains relatively modest, which is not uncommon in systems where hydrophobic or van der Waals interactions also play substantial roles in stabilizing the complex [110]. Notably, the slightly higher frequency and number of hydrogen bonds in the 5GS4_PCB2 system indicates marginally stronger or more dynamic intermolecular interaction compared to the 5GS4_PCB system. The quality of the simulation

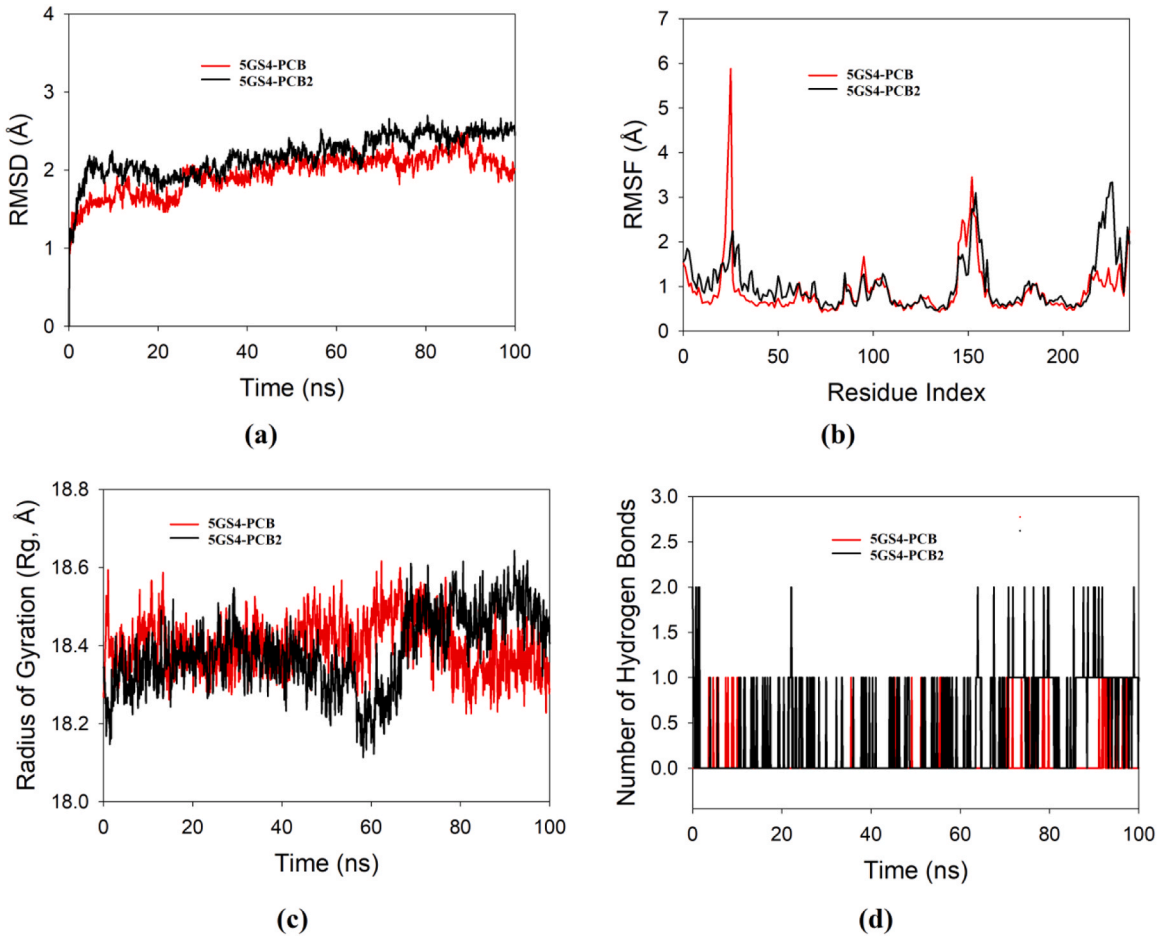

Fig. 5. (a) RMSD (b) RMSF (c) Rg (d) Number of hydrogen bonds for PCB and PCB2.

appears robust, as indicated by the absence of unnatural surges or prolonged absences of hydrogen bonds, supporting a consistent and realistic depiction of biomolecular behavior under simulated conditions.

The SASA is a parameter in MD simulations, offering a measure of the surface area of a biomolecule accessible to solvent molecules and thus reflecting conformational dynamics and interaction behavior upon ligand binding. In the provided SASA plot (Fig. 6), the receptor (5GS4) in its unbound (red line) and ligand-bound (black line) states is monitored over the course of 1000 simulation frames. The unbound receptor consistently exhibits a higher SASA, averaging between 450–550 Å^2, indicating a more solvent-exposed conformation. In contrast, the receptor bound to the PCB ligand maintains a notably lower SASA, predominantly within the range of 300–400 Å^2, signifying reduced solvent exposure due to complex formation. This marked reduction in SASA upon ligand binding suggests that the interaction induces a more compact conformation or shields solvent-accessible regions of the receptor, enhancing its structural stability. Throughout the simulation, both states exhibit mild fluctuations — a natural outcome of protein dynamics — but no significant spikes or destabilizing deviations are observed, reflecting a high-quality, equilibrated simulation. Such SASA behavior is typical of stable protein-ligand complexes, corroborating previous findings where ligand binding reduces solvent exposure,

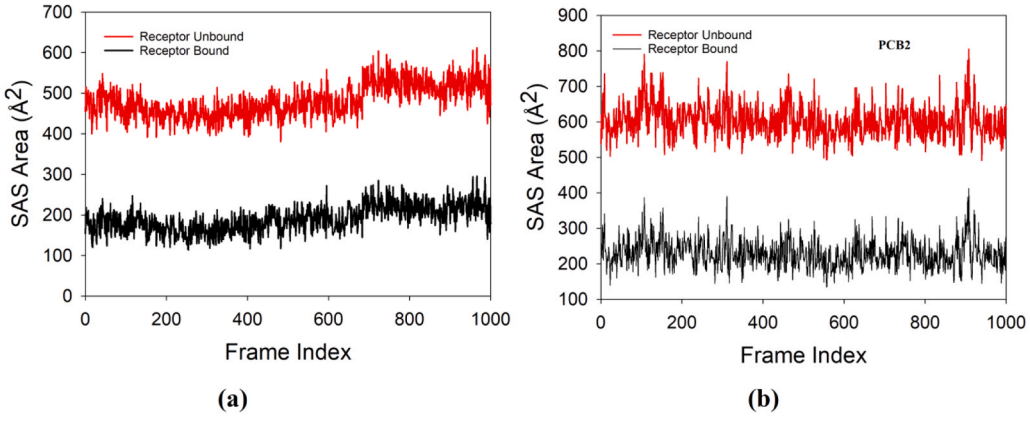

Fig. 6. SASA plots (a) 5GS4 and 5GS4-PCB (b) 5GS4 and 5GS4-PCB2.

contributing to structural stabilization [111]. In the presented SASA plot for the 5GS4 protein, monitored across 1000 simulation frames, the behavior of the unbound receptor (red line) is compared to its conformation when bound to the PCB2 ligand (black line). The unbound state consistently exhibits higher SASA values, predominantly fluctuating between 600–800 Å^2, indicating a more solvent-exposed and conformationally open protein structure. In contrast, the receptor-ligand complex maintains notably lower SASA values, ranging around 200–350 Å^2, throughout the simulation. This substantial reduction in solvent exposure upon ligand binding reflects a clear compaction of the protein structure and the partial burial of residues at the binding interface, stabilizing the complex and reducing its dynamic flexibility. The relatively consistent SASA profile of the bound state, with no excessive fluctuations or spikes, highlights the stability and equilibration quality of the simulation. These findings align with established MD simulation outcomes, where ligand-induced reductions in SASA correlate with increased structural compactness and stabilization of protein-ligand complexes [112], supporting the robustness of the modeled interactions in this system.

For the 5GS4 bound to PCB, the binding free energy (BE) and additional energies in the form of MM-GBSA were calculated using MD simulation trajectory (Table 5). MM/GBSA BE components for the 5GS4 bound to PCB and PCB2 are in Table 5. ΔGbind for the 5GS4-PCB is slightly more favorable at −58.45 compared to −56.61 for 5GS4-PCB2, suggesting that while both ligands form stable complexes, PCB displays marginally higher affinity for the receptor. Subtle variations in interaction characteristics are revealed by breaking down the energies. Stronger hydrophobic contacts for PCB are indicated by the much more favorable ΔGbindLipo contribution in the 5GS4-PCB complex (-26.22) compared to the 5GS4-PCB2 (-15.23). On the other hand, PCB2 (-23.21) exhibits much more favorable ΔGbindvdW interactions than PCB (-14.45), suggesting a tighter steric complementarity between PCB2 and the binding pocket. Both have favorable electrostatic interactions (16.65 for PCB and 11.54 for PCB2), although the PCB2 combination is marginally less destabilizing. PCB has small but more favorable ΔGbindHbond (-4.01 vs. −2.99), which indicates that the compound has stronger hydrogen bonds. The fact that PCB2 has a lower ΔGbindSolvGB (38.12) than PCB (48.23), which usually opposes binding due to desolvation penalties, suggests improved solvation balance upon binding. PCB2 is marginally favored by packing (-7.28), although GbindCovalent and ΔGbindPacking terms are still equivalent. Overall, PCB2 compensates with superior van der Waals and solvation energy terms, indicating unique but competitive binding profiles, in line with proven MM/GBSA applications in ligand affinity prediction, even though PCB achieves greater lipophilic and hydrogen bonding interactions [113].

Table 5
Binding free energy components for the 5GS4 bound to PCB and PCB2 calculated by MM-GBSA.

Energies (kcal/mol)	5GS4 bound to PCB	5GS4 bound to PCB2
ΔG_{bind}	-58.45	-56.61
ΔG_{bind}Lipo	-26.22	-15.23
ΔG_{bind}vdW	-14.45	-23.21
ΔG_{bind}Coulomb	16.65	11.54
$\Delta G_{bind}H_{bond}$	-4.01	-2.99
ΔG_{bind}SolvGB	48.23	38.12
ΔG_{bind}Covalent	2.09	2.22
ΔG_{bind}Packing	-6.99	-7.28

4. Conclusion

This work provides a comprehensive computational assessment of Palcociclib adsorption on gold nanoclusters and its implication for sensing, electronic modulation, and biological recognition. Our DFT analysis reveals that Au_3 adsorption induces substantial charge redistribution within PCB, lowering its energy gap while enhancing polarizability and nonlinear optical response features highly desirable for optical and SERS-based sensor technologies. Spectroscopic simulations confirm strong and oriented adsorption through nitrogen and oxygen centers, while solvation studies show that these complexes remain highly stable under physiological conditions. Protein-ligand modeling further demonstrates that both PCB and PCB-Au_3 maintain stable binding within the 5GS4 receptor, with the gold-modified ligand engaging in a broader spectrum of non-covalent interactions. Although PCB exhibits slightly stronger overall binding, the Au_3-linked complex benefits from enhanced van der Waals and solvation contributions, underscoring how metal functionalization subtly tunes binding energetics. The consistent behavior across RMSD, RMSF, Rg, hydrogen bonding and SASA metrics confirms the structural reliability of both complexes over long-timescale MD simulations. Overall, our findings establish Au_3 nanoclusters as an effective platform for improving the optical detectability, stability, and biomolecular interactions of Palbociclib, opening avenues for their application in drug sensing, targeted delivery, and theranostic strategies in breast cancer management.

CRediT authorship contribution statement

Y. Sheena Mary: Writing – original draft, Software, Methodology, Formal analysis, Data curation. **Jamelah S. Al-Otaibi:** Writing – original draft, Software, Formal analysis, Data curation. **Maria Cristina Gamberini:** Writing – review & editing, Writing – original draft, Software, Formal analysis, Data curation. **A. Saral:** Writing – original draft, Software, Formal analysis, Data curation.

Declaration of Competing Interest

The authors declare no conflict of interest.

Acknowledgements

Princess Nourah Bint Abdulrahman University Researchers Supporting Project number (PNURSP2025R13), Princess Nourah Bint Abdulrahman University, Riyadh 11671, Saudi Arabia

Appendix A. Supporting information

Supplementary data associated with this article can be found in the online version at doi:10.1016/j.nanoso.2025.101597.

Data availability

Data will be made available on request.

References

[1] A. Popczyk, A. Aamoum, A. Migalska-Zalas, P. Plociennik, A. Zawadzaka, J. Mysliwiec, B. Sahraoui, Selected organometallic compounds for third order nonlinear optical application, S. Nanomater. 9 (2019) 254, https://doi.org/10.3390/nano9020254.
[2] T. Huang, Z. Hao, H. Gong, Z. Liu, S. Xiao, S. Li, Y. Zhai, S. You, Q. Wang, J. Qin, Third-order nonlinear optical properties of a new copper coordination compound: a promising candidate for all-optical switching, Chem. Phys. Lett. 451 (2008) 213–217, https://doi.org/10.1016/j.cplett.2007.12.001.
[3] U.R. Felscia, B.J.M. Rajkumar, M. Nidya, P. Sankar, Electronic and nonlinear optical properties of 1-histidine on silver: a theoretical and experimental approach, J. Phys. Chem. A 122 (2018) 1045–1052, https://doi.org/10.1021/acs.jpca.7b07493.
[4] T. Fernandes, S. Fateixa, M. Ferro, H.I.S. Nogueira, A.L. Daniel-da-Silva, T. Trindade, Colloidal dendritic nanostructures of gold and silver for SERS analysis of water pollutants, J. Mol. Liq. 337 (2021) 116608, https://doi.org/10.1016/j.molliq.2021.116608.
[5] A. Szaniawska, A. Kudelski, Applications of surface-enhanced Raman scattering in biochemical and medical analysis, Front. Chem. 9 (2021) 664134, https://doi.org/10.3389/fchem.2021.664134.
[6] U.R. Felscia, B.J.M. Rajkumar, P. Sankar, R. Philip, M.B. Mary, Optical nonlinearity and charge transfer analysis of pyrene adsorbed on silver:

computational and experimental investigations, Spectrochim. Acta 184 (2017) 286–293, https://doi.org/10.1016/j.saa.2017.05.021.
[7] N.R. Chowdhury, M. MacGregor-Ramiasa, P. Zilm, P. Majewski, K. Vasilev, Chocolate; silver nanoparticles: synthesis, antibacterial activity and cytotoxicity, J. Colloid Interface Sci. 482 (2016) 151–158, https://doi.org/10.1016/j.jcis.2016.08.003.
[8] Z. Tavaf, M. Tabatabaei, A. Khalafi-Nezhad, F. Panahi, Evaluation of antibacterial, antibofilm and antioxidant activities of synthesized silver nanoparticles (AgNPs) and casein peptide fragments against streptococcus mutans, Eur. J. Integr. Med. 12 (2017) 163–171, https://doi.org/10.1016/j.eujim.2017.05.011.
[9] K. Domeradzka-Gajda, M. Nocun, J. Roszak, B. Janasik, C.D. Quarles, Jr, W. Wasowicz, J. Grobelny, E. Tomaszewska, G. Celchowski, K.R. Soliwoda, M. Cieslak, D. Puchowicz, J.J. Gonzalez, R.E. Russo, M. Stepnik, A study on the in vitro percutaneous absorption of silver nanoparticles in combination with aluminum chloride, methyl paraben or di-n-butyl phthalate, Toxicol. Lett. 272 (2017) 38–48, https://doi.org/10.1016/j.toxlet.2017.03.006.
[10] M.E.K. Kraeling, V.D. Topping, Z.M. Keltner, K.R. Belgrave, K.D. Bailey, X. Gao, J. J. Yourick, In vitro percutneous penetration of silver nanoparticles in pig and human skin, Regul. Toxicol. Pharm. 95 (2018) 314–322, https://doi.org/10.1016/j.yrtph.2018.04.006.
[11] E. Fortunati, M. Peltzer, I. Armentano, A. Jimenez, J.M. Kenny, Combined effects of cellulose nanocrystals and silver nanoparticles on the barrier and migration properties of pla nano-biocomposites, J. Food Eng. 118 (2013) 117–124, https://doi.org/10.1016/j.jfoodeng.2013.03.025.
[12] S. Kumar, A. Shukla, P.P. Baul, A. Mitra, D. Halder, Biodegradable hybrid nanocomposities of chitosan/gelatin and silver nanoparticles for active food packaging applications, Food Packag. Shelf 16 (2018) 178–184, https://doi.org/10.1016/j.fpsl.2018.03.008.
[13] B. Pannerselvam, M.K.D. Jothinathan, M. Rajendran, P. Perumal, K. P. Thangavelu, H.J. Kim, V. Singh, S.K. Rangarajulu, An in vitro study on the burn wound healing activity of cotton fabrics incorporated with phytosynthesized silver nanoparticles in male Wistar albino rats, Eur. J. Pharm. Sci. 100 (2017) 187–196, https://doi.org/10.1016/j.ejps.2017.01.015.
[14] Y. Zhou, R.C. Tang, Facile and eco-friendly fabrication of AgNPs coated silk for antibacterial and antioxidant textiles using honeysuckle extract, J. Photochem. Photobiol. B 178 (2018) 463–471, https://doi.org/10.1016/j.jphotobiol.2017.12.003.
[15] L. Zhang, G. Zeng, H. Dong, Y. Chen, J. Zhang, M. Yan, Y. Zhu, Y. Yuan, Y. Xie, Z. Huang, The impact of silver nanoparticles on the co-composting of sewage sludge and agricultural waster: evolutions of organic matter and nitrogen, Bioresour. Technol. 230 (2017) 132–139, https://doi.org/10.1016/j.biortech.2017.01.032.
[16] S.D. Gupta, A. Agarwal, S. Pradhan, Phytostimulatory effect of silver nanoparticles (AgNPs) on rice seedling growth: an insight from antioxidative enzyme activities and gene expression pattersn, Ecotoxicol. Environ. Saf. 161 (2018) 624–633, https://doi.org/10.1016/j.ecoenv.2018.06.023.
[17] R. Wen, Y. Fang, Adsorption of pyridine carboxylic acids on silver surface investigated by potential-dependent SERS, Vib. Spectrosc. 39 (2005) 106–113, https://doi.org/10.1016/j.vibspec.2005.01.001.
[18] L.R. Wang, Y. Fang, Experimental (UV-Raman) and theoretical (DFT) study of pyridine carboxylic acid in aqueous solution, Chem. Phys. 323 (2006) 376–382, https://doi.org/10.1016/j.chemphys.2005.10.001.
[19] M. Moskovits, Metal clusters, Annu. Rev. Phys. Chem. 42 (1991) 465–499, https://doi.org/10.1146/annurev.pc.42.100191.002341.
[20] U. Heiz, W.-D. Schneider, Nanoassembled model catalysts, J. Phys. D Appl. Phys. 33 (2000) R85–R102, https://doi.org/10.1088/0022-3727/33/11/201.
[21] Z. Zhao, M.A. Carpenter, Support-free bimodal distribution of plasmonically active Ag/AgO_x nanoparticle catalysts: attributes and Plasmon enhanced surface chemistry, J. Phys. Chem. C 117 (2013) 11124–11132, https://doi.org/10.1021/jp400837r.
[22] F. Petronella, E. Fanizza, G. Mascolo, V. Locaputo, L. Bertinetti, G. Martra, S. C. Coluccia, A. Agostiano, M.L. Curri, R. Comparelli, Photocatalytic activity of nanocomposite catalyst films based on nanocrystalline metal/semiconductors, J. Phys. Chem. C 115 (2011) 12033–12040, https://doi.org/10.1021/jp201098t.
[23] H. Gorter, M.J.J. Coenen, M.W.L. Slaats, M. Ren, W. Lu, C.J. Kuijpers, W. A. Groen, Toward inkjet printing of small molecule organic light emitting diodes, Thin Solid Films 532 (2013) 11–15, https://doi.org/10.1016/j.tsf.2013.01.041.
[24] C.-T. Lin, C.-H. Hsu, C.-H. Lee, W.-J. Wu, Inkjet-printed organic field-effect transistor by using composite semiconductor material of carbon nanoparticles and poly(3-hexylthiophene), J. Nanotechnol. 2011 (2011) 142890, https://doi.org/10.1155/2011/142890.
[25] G. Frenking, N.F. Rohlich, The nature of the bonding in transition-metal compounds, Chem. Rev. 100 (2000) 717–774, https://doi.org/10.1021/cr9804011.
[26] S. Ogut, J.C. Idrobo, J. Jellinek, J. Wang, Structural, electronic, and optical properties of noble metal clusters from first principles, J. Clust. Sci. 17 (2006) 609–626, https://doi.org/10.1007/s10876-006-0075-8.
[27] E. Lim, J. Heo, X. Zhang, K.H. Bowen, S.H. Lee, S.K. Kim, Anionic activation of CO_2 via (Mn-CO_2)-complex on magic-numbered anionic coinage metal clusters Mb-(M=Cu, Ag, Au), J. Phys. Chem. A 125 (2021) 2243–2248, https://doi.org/10.1021/acs.jpca.0c10867.
[28] N. Agarwal, S.K. Raghuwanshi, D. Upadhyay, P. Shukla, V.J. Ram, Suitably functionalized pyrimidines as potential antimycotic agents, Bioorg. Med. Chem. Lett. 19 (2000) 703–706, https://doi.org/10.1016/s0960-894x(00)00091-3.
[29] P. Sharma, N. Rane, V. Gurram, Synthesis and QSAR studies of pyrimido[4,5-d] pyrimidine-2,5-dione derivatives as potential antimicrobial agents, Bioorg. Med. Chem. Lett. 14 (2004) 4185–4190, https://doi.org/10.1016/j.bmcl.2004.06.014.
[30] G.L. Amidon, H. Lenneernas, C.P. Shah, J.R. Crison, A theoretical basis for a biopharmaceutic drug classification: the correlation of in vitro drug product dissolution and in vivo bioavailability, Pharm. Res. 12 (1995) 413–420, https://doi.org/10.1023/a:1016212804288.
[31] X. Yang, S. Li, Q.-W. Zhang, Y. Zheng, D. Bardelang, L.-H. Wang, R. Wang, Concealing the taste of the guinnes world's most bitter substance by using a synthetic nanocontainer, Nanoscale 9 (2017) 10606–10609, https://doi.org/10.1039.c7nr03608f.
[32] D. Katiyar, S. Ahmad, S.G. Dash, S. Tripathi, A. Arora, T.S. Thakur, Understanding the guest binding in the cucurbit[7]uril inclusion complexes of CDK4/6 inhibitors, palbociclib, and ribociclib from a combined experimental and computational study, J. Mol. Struct. 1241 (2021) 130637, https://doi.org/10.1016/j.molstruc.2021.130637.
[33] G. Magdy, M.A. Shaldam, F. Belal, H. Elmansi, Multi spectroscopic, thermodynamic, and molecular docking/dynamic approaches for characterization of the binding interaction between calf thymus DNA and palbociclib, Sci. Rep. 12 (2022) 14723, https://doi.org/10.1038/s41598-022-19015-9.
[34] F. Serra, P. Lapidari, E. Quaquarini, B. Tagliaferri, F. Sottotetti, R. Palumbo, Palbociclib in metastatic breast cancer: current evidence and real life data, Drugs Context 8 (2019) 212579, https://doi.org/10.7573/dic.212579.
[35] Y. Zhang, C. Wu, N. Zhang, R. Fan, Y. Ye, J. Xu, Recent advances in the development of pyrazole derivatives as anticancer agents, Int. J. Mol. Sci. 24 (2023) 12724, https://doi.org/10.3390/ijms241612724.
[36] A. Monteiro, L.M. Goncalves, M.M.M. Santos, Synthesis of novel spiropyrazoline oxindoles and evaluation of cytotoxicity in cancer cell lines, Eur. J. Med. Chem. 79 (2014) 266–272, https://doi.org/10.1016/j.ejmech.2014.04.023.
[37] A. Khaldan, S. Bouamrane, R. El-Mernissi, M. Alaqarbeh, H. Maghat, M. Bouachrine, T. Lakhlifi, A. Sbai, Integrated computer aided methods to designing potent α-glucosidase inhibitors based on quinoline scaffold derivative, S. Curr. Chem. Lett. 14 (2025) 79–106, https://doi.org/10.5267/j.ccl.2024.9.003.
[38] S. Bouamrane, A. Khaldan, M. Alaqarbeh, A. Sbai, M.A. Ajana, M. Bouachrine, T. Lakhlifi, H. Maghat, Garlic as an effective antifungal inhibitor: a combination of reverse docking, molecular dynamics simulation, ADMET screening, DFT, and retrosynthesis studies, Arab. J. Chem. 17 (2024) 105642, https://doi.org/10.1016/j.arabjc.2024.105642.
[39] S. Bouamrane, A. Khaldan, M. Alaqarbeh, A. Sbai, M.A. Ajana, T. Lakhlifi, M. Bouachrine, H. Maghat, Computational integration for antifungal 1,2,4-triazole inhibitors design: QSAR, molecular docking, molecular dynamics simulations, ADME/Tox, and retrosynthesis studies, Chem. Phys. Impact 8 (2024) 100502, https://doi.org/10.1016/j.chphi.2024.100502.
[40] A. Khaldan, S. Boumrane, R. El-Mernissi, H. Maghat, M.A. Ajana, A. Sbai, M. Bouachrine, T. Lakhlifi, In silico study of 2,4,5-trisubstituted thiazoles as inhibitors of tuberculosis using 3D-QSAR, molecular docking, and ADMET analysis, ElCezeri J.. Sci. Eng. 9 (2022) 452–468, https://doi.org/10.31202/ecjse.961940.
[41] V.V. Aswathy, Y.S. Mary, P.J. Jojo, C.Y. Panicker, A. Bielenica, S. Armakovic, S. J. Armakovic, P. Brzozka, S. Krukowski, C. Van Alsenoy, Investigation of spectroscopic, reactive, transport and docking properties of 1-(3,4-dichlorophenyl)-3-[3-(trifluoromethyl)phenyl]thiourea (ANF-6): Combined experimental and computational study, J. Mol. Struct. 1134 (2017) 668–680, https://doi.org/10.1016/j.molstruc.2017.01.016.
[42] U.R. Felscia, B.J.M. Rajkumar, M.B. Mary, Theoretical investigations on nonlinear fused 4-ring systems: application to OLED and NLO devices, Synth. Met. 246 (2018) 31–38, https://doi.org/10.1016/j.synthmet.2018.09.008.
[43] S. Premkumar, A. Jawahar, T. Mathavan, M.K. Dhas, A.M.F. Benial, Vibrational spectroscopic and nonlinear optical activity studies on nicotinanilide: a DFT approach, AIP Conf. Proc. 1665 (2015) 140041, https://doi.org/10.1063/1.4918250.
[44] J.N. Latosinska, M. Latosinska, M.A. Tomczak, Conformational stability and thermal pathways of relaxation in triclosan (antibacterial/excipient/contaminant) in solid-state: combined spectroscopic (^{1}H NMR) and computational (periodic DFT) study, J. Phys. Chem. A 119 (2015) 4864–4874, https://doi.org/10.1021/acs.jpca.5b02393.
[45] S. Dorotikova, K. Plevova, L. Bucinsky, M. Malcek, P. Herich, L. Kuckova, M. Bobenicova, S. Soralova, J. Kozisek, M. Fronc, V. Milata, D. Dvoranova, Conformational, spectroscopic, and molecular dynamics DFT study of precursors for new potential antibacterial fluoroquinolone drugs, J. Phys. Chem. A 118 (2014) 9540–9551, https://doi.org/10.1021/jp506355f.
[46] A. Irfan, M. Imran, R. Thomas, M.A.R. Basra, S. Ullah, A.G. Al-Sehemi, M. A. Assiri, Exploring the effect of oligothiophene and acene cores on the optoelectronic properties and enhancing p- and n-type ability of semiconductor materials, J. Sulfur Chem. 42 (2021) 180–192, https://doi.org/10.1080/17415993.2020.1830401.
[47] J.S. Al-Otaibi, Y.S. Mary, Y.S. Mary, R. Thomas, Evidence of cluster formation of pyrrole with mixed silver metal clusters, Agx-My (x=4,5, Y=2/1 and M=Au/Ni/Cu) using DFT/SERS analysis, Comput. Theor. Chem. 1208 (2022) 113569, https://doi.org/10.1016/j.comptc.2021.113569.
[48] J.S. Al-Otaibi, Y.S. Mary, Y.S. Mary, Z. Ullah, H.W. Kwon, Adsorption behavior and solvent effects of an adamantane-triazole derivative on metalclusters-DFT simulation studies, J. Mol. Liq. 345 (2022) 118242, https://doi.org/10.1016/j.molliq.2021.118242.

[49] J.S. Al-Otaibi, Y.S. Mary, Y.S. Mary, Z. Ullah, R. Yadav, N. Gupta, D.G. Churchill, Adsorption properties of dacarbazine with graphene/fullerene/metal nanocages-reactivity, spectroscopic and SERS analysis, Spectrochim. Acta 268 (2021) 120677, https://doi.org/10.1016/j.saa.2021.120677.
[50] J.S. Al-Otaibi, Y.S. Mary, Y.S. Mary, Adsorption of a thione bioactive derivative over different silver/gold clusters – DFT investigations, Comput. Theor. Chem. 1207 (2022) 113497, https://doi.org/10.1016/j.comptc.2021.113497.
[51] J.S. Al-Otaibi, Y.S. Mary, Y.S. Mary, R. Trivedi, B. Chakraborty, Theoretical investigation on the adsorption of melamine in Al12/B12-N12/P12 fullerene-like nanocages: a platform for ultrasensitive detection of melamine, Chem. Pap. 76 (2022) 225–238, https://doi.org/10.1007/s11696-021-01849-8.
[52] J.S. Al-Otaibi, Y.S. Mary, Y.S. Mary, R. Thomas, Evidence of cluster formation of croconic acid with Ag, Au and Cu cages, enhancement of electronic properties and Raman activity, Spectrochim. Acta 264 (2022) 120233, https://doi.org/10.1016/j.saa.2021.120233.
[53] P. Albrycht, J.S. Al-Otaibi, Y.S. Mary, Y.S. Mary, R. Trivedi, B. Chakraborty, Surface enhanced Raman scattering investigation of pioglitazone on silver and silver-gold substrates-Experimental analysis and theoretical modeling, J. Mol. Struct. 1244 (2021) 130992, https://doi.org/10.1016/j.molstruc.2021.130992.
[54] Y.S. Mary, Y.S. Mary, S. Armakovic, S.J. Armakovic, R. Yadav, I. Celik, P. Mane, B. Chakraborty, Stability and reactivity study of bio-molecules brucine and colchicines towards electrophile and nucleophile attacks: insight from DFT and MD simulations, J. Mol. Liq. 335 (2021) 116192, https://doi.org/10.1016/j.molliq.2021.116192.
[55] J.S. Al-Otaibi, Y.S. Mary, Y.S. Mary, R. Trivedi, B. Chakraborty, R. Yadav, I. Celik, S. Soman, DFT and MD investigations of the biomolecules of phenothiazine derivatives: interactions with gold and water molecules and investigation in search of effective drug for SARS-CoV-2, J. Biomol. Struct. Dyn. 41 (2023) 4522–4533, https://doi.org/10.1080/07391102.2022.2068649.
[56] Gaussian 16, Revision A.03, M.J. Frisch, G.W. Trucks, H.B. Schlegel, G.E. Scuseria, M.A. Robb, J.R. Cheeseman, G. Scalmani, V. Barone, G.A. Petersson, H. Nakatsuji, X. Li, M. Caricato, A.V. Marenich, J. Bloino, B.G. Janesko, R. Gomperts, B. Mennucci, H.P. Hratchian, J.V. Ortiz, A.F. Izmaylov, J.L. Sonnenberg, D. Williams-Young, F. Ding, F. Lipparini, F. Egidi, J. Goings, B. Peng, A. Petrone, T. Henderson, D. Ranasinghe, V.G. Zakrzewski, J. Gao, N. Rega, G. Zheng, W. Liang, M. Hada, M. Ehara, K. Toyota, R. Fukuda, J. Hasegawa, M. Ishida, T. Nakajima, Y. Honda, O. Kitao, H. Nakai, T. Vreven, K. Throssell, J.A. Montgomery, Jr., J.E. Peralta, F. Ogliaro, M.J. Bearpark, J.J. Heyd, E.N. Brothers, K.N. Kudin, V.N. Staroverov, T.A. Keith, R. Kobayashi, J. Normand, K. Raghavachari, A.P. Rendell, J.C. Burant, S.S. Iyengar, J. Tomasi, M. Cossi, J.M. Millam, M. Klene, C. Adamo, R. Cammi, J.W. Ochterski, R.L. Martin, K. Morokuma, O. Farkas, J.B. Foresman, D.J. Fox, Gaussian, Inc., Wallingford CT, 2016.
[57] J.Y. Zhao, Y. Zhang, L. Zhu, Theoretical studies on vibrational spectra of mixed cyanide-halide complexes of gold (III), J. Mol. Struct. Theochem. 671 (2004) 179–187, https://doi.org/10.1016/j.theochem.2003.10.065.
[58] GaussView, Version 6.1, R. Dennington, T.A. Keith, J.M. Millam, Semichem Inc., Shawnee Mission, KS, 2016.
[59] https://prankweb.cz/ .
[60] D.E. Shaw, P. Maragakis, K. Lindorff-Larsen, S. Piana, R.O. Dror, M.P. Eastwood, J.A. Bank, J.M. Jumper, J.K. Salmon, Y. Shan, W. Wriggers, Atomic-level characterization of the structural dynamics of proteins, Science 330 (2010) 341–346, https://doi.org/10.1126/science.1187409.
[61] W.L. Jorgensen, J. Chandrasekhar, J.D. Madura, R.W. Impey, M.L. Klein, Comparison of simple potential functions for simulating liquid water, J. Chem. Phys. 79 (1983) 926–935, https://doi.org/10.1063/1.445869.
[62] W.L. Jorgensen, J. Tirado-Rives, The OPLS [optimized potentials for liquid simulations potential functions for proteins, energy minimizations for crystals of cyclic peptides and crambin, J. Am. Chem. Soc. 110 (1988) 1657–1666, https://doi.org/10.1021/ja00214a001.
[63] J.S. Rani, U.R. Felscia, S.W.N. Eastman, D. Yamini, Theoretical investigations on structural, optical and vibrational properties of pyridine 3-carboxylic acid adsorbed on a silver cluster, J. Electron. Mater. 51 (2022) 3970–3979, https://doi.org/10.1007/s11664-022-09638-z.
[64] A. Rahmanzadeh, M. Rezvani, M.D. Ganji, M.T. Moghim, Corrosion protection performance of laurhydrazide N′-propan-3-one (LHP) adsorbed on zinc surface: a DFT-MD simulation investigation, Mater. Commun. 36 (2023) 106946, https://doi.org/10.1016/j.mtcomm.2023.106946.
[65] H. Ullah, K. Ayub, Z. Ullah, M. Hanif, R. Nawas, A.A. Shah, S. Bilal, Theoretical insight of polypyrrole ammonia gas sensor, Synth. Met. 172 (2013) 14–20, https://doi.org/10.1016/j.synthmet.2013.03.021.
[66] J.G. Brandenburg, M. Alessio, B. Civalleri, M.F. Peintinger, T. Bredow, S. Grimme, Geometrical correction for the inter- and intramolecular basis set superposition error in periodic density functional theory calculations, J. Phys. Chem. A 117 (2013) 9282–9292, https://doi.org/10.1021/jp406658y.
[67] https://wwwtc.thch.uni-bonn.de/ .
[68] L. Kruse, L. Goerigk, S. Grimme, Why the standard B3LYP/6–31G* model chemistry should not be used in DFT calculations of molecular thermochemistry: understanding and correcting the problem, J. Org. Chem. 77 (2012) 10824–10834, https://doi.org/10.1021/jo302156p.
[69] B. Sureshkumar, Y.S. Mary, K.S. Resmi, C.Y. Panicker, S. Armakovic, S. J. Armakovic, C. Van Alsenoy, B. Narayana, S. Suma, Spectroscopic analysis of 8-hydroxyquinoline derivatives and investigation of its reactive properties by DFT and molecular dynamics simulations, J. Mol. Struct. 1156 (2018) 336–347, https://doi.org/10.1016/j.molstruc.2017.11.120.
[70] P. Sangeetha, S. Mullainathan, L. Rajasekaran, S. Muthu, A. Irfan, A. Saral, Electronic properties of solvents (water, benzene, ethanol) using IEFPCM model, spectroscopic exporation with drug likeness and assessment of molecular docking on 1-octanesulfnic acid sodium salt, J. Mol. Liq. 344 (2021) 117719, https://doi.org/10.1016/j.molliq.2021.117719.
[71] J.S. Al-Otaibi, A.H. Almuqrin, Y.S. Mary, R. Thomas, Modeling the conformational preference, spectroscopic properties, UV light harvesting efficiency, biological receptor inhibitory ability and other physico-chemical properties of five imidazole derivatives using quantum mechanical and molecular mechanics tools, J. Mol. Liq. 310 (2020) 112871, https://doi.org/10.1016/j.molliq.2020.112871.
[72] N.P.G. Roeges, A Guide to the Complete Interpretation of Infrared Spectra of Organic Structures, John Wiley and Sons Inc, New York, 1994.
[73] Y.S. Mary, C.Y. Panicker, T.S. Yamuna, M.S. Siddegowda, H.S. Yathirajan, A. A. Al-Saadi, C. Van Alsenoy, Theoretical investigations on the molecular structure, vibrational spectral, HOMO-LUMO and NBO analysis of 9-[3-(dimethylamino)propyl]-2-trifluoro-methyl-9H-thioxanthen-9-ol, Spectrochim. Acta 132 (2014) 491–501, https://doi.org/10.1016/j.saa.2014.05.016.
[74] D.L. Pavia, G.M. Lampman, G.S. Kriz. Introduction to Spectroscopy, third edition, Thomson Learning, Inc, 2001, p. 579.
[75] K. Arulaabaranam, S. Muthu, G. Mani, A. Irfan, Conformational study, FT-IR, FT-Raman, solvent effect on UV-Vis, charge transfer and protein-ligand interactions of methyl-2-pyrazine carboxylate, J. Mol. Liq. 341 (2021) 116934, https://doi.org/10.1016/j.molliq.2021.116934.
[76] A. Mahmood, S.U.D. Khan, U.A. Rana, Theoretical designing of novel heterocyclic azo dyes for dye sensitized solar cells, J. Comput. Electron 13 (2014) 1033–1041, https://doi.org/10.1007/s10825-014-0628-2.
[77] A. Mahbood, S.U.D. Khan, F. Ur Rehman, Assessing the quantum mechanical level of theory for prediction of UV/Visible absorption spectra of some aminoazobenzene dyes, J. Saudi Chem. Soc. 19 (2015) 436–441, https://doi.org/10.1016/j.jscs.2014.06.001.
[78] A. Mahmood, S.U.D. Khan, U.A. Rana, M.H. Tahir, Red shifting of absorption maxima of phenothiazine based dyes by incorporating electron-deficient thiadiazole derivatives as π-spacer, Arab. J. Chem. 12 (2019) 1447–1453, https://doi.org/10.1016/j.arabjc.2014.11.007.
[79] S.U.D. Khan, A. Mahmood, U.A. Rana, S. Haider, Utilization of electron-deficient thiadiazole derivatives as π-spacer for the red shifting of absorption maxima of diarylamine-fluorene based dyes, Theor. Chem. Acc. 134 (2015) 1596, https://doi.org/10.1007/s00214-014-1596-0.
[80] Y.S. Mary, Y.S. Mary, K.S. Resmi, V.S. Kumar, R. Thomas, B. Sureshkumar, Detailed quantum mechanical, molecular docking, QSAR prediction, photovoltaic light harvesting efficiency analysis of benzyl and its halogenated derivatives, Heliyon 5 (2019) e02825, https://doi.org/10.1016/j.heliyon.2019.e02825.
[81] J.S. Al-Otaibi, Y.S. Mary, Y.S. Mary, G. Serdaroglu, Adsorption of adipic acid in Al/B-N/P nanocages: DFT investigations, J. Mol. Model. 27 (2021) 113, https://doi.org/10.1007/s00894-021-04742-z.
[82] S. Sarala, S.K. Geetha, S. Muthu, A. Irfan, Theoretical investigation on influence of protic and aprotic solvent effect and structural (monomer, dimer), Van der Waals and Hirshfeld surface analysis for clonidine molecule, Comput. Theor. Chem. 1204 (2021) 113397, https://doi.org/10.1016/j.comptc.2021.113397.
[83] S. Hosna, D.E. Janzen, Y.S. Mary, K.S. Resmi, R. Thomas, R. Mohamed, S. Wajda, Molecular structure, spectroscopic, dielectric and thermal study, nonlinear optical properties, natural bond orbital, HOMO-LUMO and molecular docking analysis of $(C_6Cl_2O_4)$ $(C_{10}H_{14}N_2F)_2{\cdot}2H_2O$, Spectrochim. Acta 204 (2018) 328–339, https://doi.org/10.1016/j.saa.2018.06.062.
[84] M. Mohammadzaheri, S. Jamehbozorgi, M.D. Ganji, M. Rezvani, Z. Javanshir, Toward functionalization of ZnO nanotubes and monolayers with 5-aminolevulinic acid drugs as possible nanocarriers for drug delivery: a DFT based molecular dynamic simulation, Phys. Chem. Chem. Phys. 25 (2023) 21492–21508, https://doi.org/10.1039/D3CP01490H.
[85] S. Vadalkar, D. Chodvadiya, N.N. Som, K.N. Vyas, P.K. Jha, B. Chakraborty, An ab initio study of the C18 nanocluster for hazardous gas sensor application, ChemistrySelect 7 (2022) e202103874, https://doi.org/10.1002/slct.202103874.
[86] A.S. Rad, First principles study of Al-doped graphene as nanostructure adsorbent for NO2 and N2O: DFT calculations, Appl. Surf. Sci. 357 (2015) 1217–1224, https://doi.org/10.1016/j.apsusc.2015.09.168.
[87] Y.S. Mary, Y.S. Mary, Utilization of doped/undoped graphene quantum dots for ultrasensitive detection of duphaston, a SERS platform, Spectrochim. Acta 244 (2021) 118865, https://doi.org/10.1016/j.saa.2020.118865.
[88] Y.S. Mary, Y.S. Mary, M. Kratky, J. Vinsova, C. Baraldi, M.C. Gamberini, DFT, molecular docking and SERS (concentration and solvent dependent) investigations of amethylisoxazole derivative with potential antimicrobial activity, J. Mol. Struct. 1232 (2021) 130034, https://doi.org/10.1016/j.molstruc.2021.130034.
[89] Y.S. Mary, Y.S. Mary, S. Armakovic, S.J. Armakovic, M. Kratky, J. Vinsova, C. Baraldi, M.C. Gamberini, Concentration and solvent dependent SERS, DFT, MD simulations and molecular docking studies of a thioxothiazolidine derivative with antimicrobial properties, J. Mol. Liq. 329 (2021) 115582, https://doi.org/10.1016/j.molliq.2021.115582.
[90] C. Reichardt, T. Welton, Sovents and Solvent Effects in Organic Chemistry, Wiley-VCH, Marburg, Germany, 2011.
[91] F. Honarasa, S. Yousefinejad, M. Nekoeinia, Structure-solubility and solvation energy relationships for propanol in different solvents using structural and empirical scales, J. Chin. Chem. Soc. 68 (2021) 1604–1616, https://doi.org/10.1002/jccs.202100215.
[92] A.R. Katritzyky, A.A. Oliferenko, P.V. Oliferenko, R. Petrukhin, D.B. Tatham, U. Maran, A. Lomaka, W.E. Acree Jr, A general treatment of solubility.1. The QSPR correlation of solvation free energies of single solutes in series of solvents,

J. Chem. Inf. Comput. Sci. 43 (2003) 1794–1805, https://doi.org/10.1021/ci034120c.
[93] Y. Shen, A. Farajtabar, J. Xu, J. Wang, Y. Xia, H. Zhao, R. Xu, Thermodynamic solubility modeling, solvent effect and preferential solvation of curcumin in aqueous co-solvent mixtures of ethanol, n-propanol, isopropanol and propylene glycol, J. Chem. Thermodyn. 131 (2019) 410–419, https://doi.org/10.1016/j.jct.2018.11.022.
[94] Z. Ullah, B. Mustafa, H.J. Kim, Y.S. Mary, Y.S. Mary, H.W. Kwon, DFT of 4-fluoro-2-oxo-1H-pyrazine-3-carboxamide (OPC) adsorption, spectroscopic, solvent effect and SERS analysis, J. Mol. Liq. 357 (2022) 119076, https://doi.org/10.1016/j.molliq.2022.119076.
[95] J.S. Al-Otaibi, Y.S. Mary, Y.S. Mary, DFT analysis of valproic acid adsorption onto Al12/B12-N12/P12 nanocages with solvent effects, J. Mol. Model 28 (2022) 98, https://doi.org/10.1007/s00894-05088-w.
[96] T. Lu, F. Chen, Multiwfn: A Multifunctional Wavefunction Analyzer (Version 3.8), 2024, Sobereva. Retrieved from ⟨https://sobereva.com/multiwfn/misc/Multiwfn_3.8_dev.pdf⟩.
[97] T. Lu, F. Chen, The electron localization function and the chemical interpretation of Fermi orbital descriptors, J. Chem. Phys. 162 (2024) 144105, https://doi.org/10.1063/5.0263003.
[98] T. Lu, F. Chen, Structure of molecule, density gradient, orbital locator and reactivity: A DFT study on benzo[d]imidazole derivative, J. Mol. Struct. 1280 (2024) 134890, https://doi.org/10.1016/j.molstruc.2023.134890.
[99] T. Lu, F. Chen, Spectroscopic, quantum chemical, and topological calculations of molecular systems, Sci. Rep. 14 (2024) 81633, https://doi.org/10.1038/s41598-024-81633-2.
[100] C. Guerra, J. Burgos, L. Ayarde-Henriquez, E. Chamorro, Formulating reduced density gradient approaches for noncovalent interactions, ChemRxiv (2024), https://doi.org/10.26434/chemrxiv-2024-bgpj2-v2.
[101] J. Siqi, Y. Shasha, W. Xiao, W. Gu, T-graphene and its boron nitride analogue as versatile drug delivery systems, Mol. Phys. 118 (2020) e1757775, https://doi.org/10.1080/00268976.2020.1757775.
[102] A.A. Peyghan, H.L. Hadipour, Z. Bagheri, Effects of Al doping and double antisite defect on the adsorption of HCN on a BC2N nanotube: density functional theory studies, J. Phys. Chem. C 117 (2013) 2427–2432, https://doi.org/10.1021/jp312503h.
[103] M.D. Ganji, H. Ko, S. Jamehbozorgi, M. Tajbakhsh, S. Tanreh, R.P. Nejad, M. Sepahvand, M. Rezvani, Unravelling performance of honeycomb structures as drug delivery systems for the isoniazid drug using DFT-D3 correction dispersion and molecular dynamic simulations, Phys. Chem. Chem. Phys. 26 (2024) 14018–14036, https://doi.org/10.1039/D3CP05457H.
[104] A. Grossfield, P.N. Patrone, D.R. Roe, A.J. Schultz, D.W. Siderius, D. M. Zuckerman, Best practices for quantification of uncertainty and sampling quality in molecular simulations [Article v1.0, Living J. Comput. Mol. Sci. 1 (2018) 5067, https://doi.org/10.3011/livecoms.1.1.5067.
[105] S.A. Hollingsworth, R.O. Dror, Molecular dynamics simulation for all, Neuron 99 (2018) 1129–1143, https://doi.org/10.1016/j.neuron.2018.08.011.
[106] G. Venkatesh, S. Haseena, J.S. Al-Otaibi, Y.S. Mary, P. Vennila, Y.S. Mary, S. A. Azad, Observations into the reactivity, docking, DFT, and MD simulations of fludarabine and clofarabine in various solvents, J. Mol. Liq. 383 (2023) 122076, https://doi.org/10.1016/j.molliq.2023.122076.
[107] R. Shukla, T. Tripathi, Molecular Dynamics Simulation of Protein and Protein-ligand Compexes. In: D.B. Singh (eds) Computer Aided Drug Design, Springer, Singapore, https://doi.org/10.1007/978-981-15-6815-2_7.
[108] J.S. Al-Otaibi, Y.S. Mary, Y.S. Mary, R. Yadav, Structural and reactivity studies of pravadoline-an ionic liquid, with reference to its wavefunction-relative properties using DFT and MD simulation, J. Mol. Struct. 1245 (2021) 131074, https://doi.org/10.1016/j.molstruc.2021.131074.
[109] M.Y. Lobanov, N.S. Bogatyreva, O.V. Galzitskaya, Radius of gyration as an indicator of protein structure compactness, Mol. Biol. 42 (2008) 701–706. PMID: 18856071.
[110] J.D. Durrant, J.A. McCammon, Molecular dynamics simulations and drug discovery, BMC Biol. 9 (2011) 71, https://doi.org/10.1186/1741-7007-0-71.
[111] M. Smitha, Y.S. Mary, Y.S. Mary, G. Serdaroglu, P. Chowdhury, M. Rana, H. Umamahesvari, B.K. Sarojini, B.J. Mohan, R. Pavithran, Modeling the DFT structural and reactivity studies of a pyrimidine-6-carboxylate derivative with reference to its wavefunction-dependent, MD simulations and evaluation for potential antimicrobial activity, J. Mol. Struct. 1237 (2021) 130397, https://doi.org/10.1016/j.molstruc.2021.130397.
[112] M. Amaral, D.B. Kokh, J. Bomke, A. Wegener, H.P. Buchstaller, H.M. Eggenweiler, P. Matias, C. Sirrenberg, R.C. Wade, M. Frech, Protein conformational flexibility modulates kinetics and thermodynamics of drug binding, Nat. Commun. 8 (2017) 2276, https://doi.org/10.1038/s41467-017-02258-w.
[113] S. Genheden, U. Ryde, The MM/PBSA and MM/GBSA methods to estimate ligand-binding affinities, Expert Opin. Drug. Discov. 10 (2015) 449–461, https://doi.org/10.1517/17460441.2015.1032936.